UC San Diego
UC San Diego Electronic Theses and Dissertations

Title

Low level optical detection of nanoparticles in blood

Permalink

https://escholarship.org/uc/item/9w3966d0

Author

McCanna, James Patrick

Publication Date

2011

Peer reviewed|Thesis/dissertation

UNIVERSITY OF CALIFORNIA, SAN DIEGO

Low Level Optical Detection of Nanoparticles in Blood

A Thesis submitted in partial satisfaction of the requirements for

the degree of Master of Science

in

Electrical Engineering (Photonics)

by

James Patrick McCanna

Committee in charge:

    Professor Sadik Esener, Chair
    Professor Michael Heller, Co-Chair
    Professor Yu-Hwa Lo
    Professor Deli Wang

2011

The Thesis of James Patrick McCanna is approved and it is acceptable in quality and form for publication on microfilm and electronically:

_____

_____

_____

Co-Chair

_____

Chair

University of California, San Diego

2011

Dedication

For my parents and grandparents. Thank you for your endless love, support, advice, and guidance.

And for my brothers. May you both find your way, as I have mine.

Epigraph

"Everyone knows that dielectrophoresis will never be used for any practical applications."

Grant Reviewer, National Institute of Health

Table of Contents

List of Abbreviations

BP	Base Pairs
CM Factor	Clausius-Mossotti Factor
CMOS	Complementary Metal Oxide Semiconductor
DNA	Deoxyribonucleic Acid
DEP	Dielectrophoresis, Dielectrophoretic
HMW	High molecular weight
KB	Kilo-base (Pairs)
NA	Numerical Aperture
TBE	Tris-Borate-EDTA
DC	Direct Current
AC	Alternating Current
PS	Polystyrene

List of Figures

List of Tables

Acknowledgements

ABSTRACT OF THE THESIS

Low Level Optical Detection of Nanoparticles in Blood

by

James Patrick McCanna

Master of Science in Electrical Engineering (Photonics)

University of California, San Diego, 2011

Professor Sadik Esener, Chair
Professor Michael Heller, Co-Chair

Common epifluorescent microscopy does not provide the sensitivity to detect low levels of important analytes, such as drug delivery nanoparticles or disease biomarkers. Advanced optical elements may be used to improve performance, but greatly increase the cost of the system. In this thesis, an epifluorescent microscope has been combined with a microelectrode array employing dielectrophoresis (DEP) to concentrate and capture nanoparticulates into defined areas; this process shown to enable low level detection below a clinically significant level. The cost of the microscope and microelectrode array analytical system is substantially lower than other advanced optical detection systems.

Chapter 1: Introduction

1.1 Motivation

The ability to detect and identify low levels of analytes is of growing importance in medicine and nanotechnology. The diagnostic monitoring of drug delivery nanoparticle levels, the identification of high molecular weight DNA in cancer patients, and the detection of potential pathogens in environmental samples are three examples where minute levels of analytes can be of extreme importance.

Common epifluorescent microscopes frequently lack the resolution and sensitivity needed to detect low levels of nanoparticulates. In comparison, modern scanning laser confocal microscopes have the ability to detect and resolve individual particles below 200 nanometers in size[1], but come with a prohibitive cost that limits widespread adoption[2]. Even if detection is possible, the ability to locate an individual particle is not guaranteed depending upon the complexity of a sample.

1.2 Inspiration

The basis for this thesis comes from a combination of research performed by other members of the Heller Lab at UCSD[3,4], and at the University of Southampton in the United Kingdom[5]. The core of this previous work involves the use of dielectrophoresis (DEP) as a robust separation technique for microscopic and nanoscopic particles. DEP is an electrokinetic process in which particles placed in an asymmetric electric field can be separated into groups by an alternating voltage signal[6,7]. DEP has the capability to separate specific nanoparticulates from interfering substances and concentrate them into a single location without additional sample preparation.

Research performed at the University of Southampton involved pairing a set of microelectrodes with a confocal microscope to serve as a micro flow cytometer. To focus target particles into a single chain, a set of four electrodes were manufactured around a fluidic capillary. Rather than using a narrowing flow channel (hydrodynamic focusing), DEP was selected to provide particle movement without affecting the flow rate and shear force in the chamber. This combined device was shown to have a particle resolution similar to commercial flow cytometers[5].

Previous work at UCSD indicated that a previous high conductance limitation to dielectrophoresis could be overcome[3,4], leading to a number of potential clinical applications. Since DEP was used to successfully approximate a flow cytometer system, its possible combination with other optical detection devices is clear. One of the most widespread optical devices is the epifluorescent microscope, commonly used in laboratory and clinical settings. The implementation of a DEP based device to enhance the capability of epifluorescent microscopy, in particular, could be a powerful tool for technicians and scientists.

1.3 Scientific Contributions

A standard reflection epifluorescent microscope employing a basic charged coupled device (CCD) camera has been paired with a fabricated microelectrode array device capable of the dielectrophoretic separation and concentration of particulates with sizes down to 20 nm. The array has been configured to allow for maximum volumetric concentration of particulates from an aqueous medium. The combined system is shown to be capable of detecting labeled nanoparticulates below the clinically significant levels

of DNA in normal blood samples (10 ng/mL) at less than one-fifth the cost of point

scanning confocal microscopes.

Chapter 2: Background and Theory

2.1 Low Level Detection via Microscopy

Fluorescent microscopy serves an important purpose in biological, medical, and engineering applications, and comes in many different forms and derivatives. A basic and popular implementation is the wide field epifluorescent microscope (Figure 1).
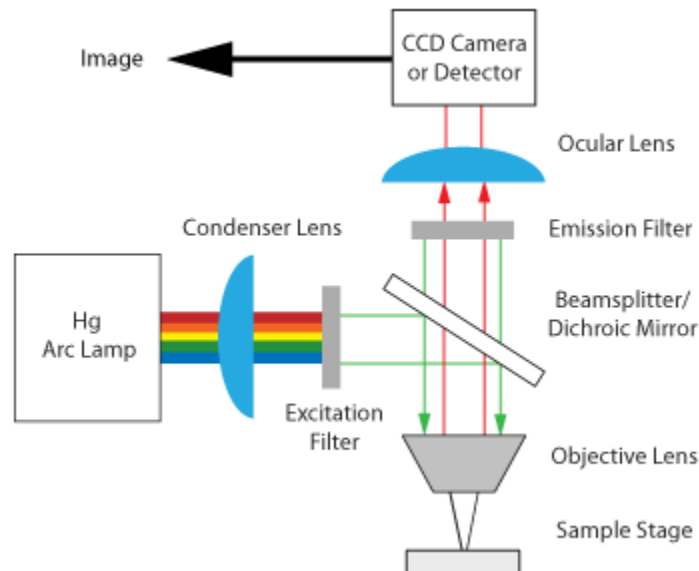
Figure 1: Epifluorescent Microscope System. System shown has been configured for reflectance imaging and employs arc lamp illumination and a CCD camera.

An epifluorescent microscope combines the smallest number of optical elements required to provide fluorescent imaging. A mercury vapor or argon arc lamp is generally employed to provide multiple illumination wavelengths without multiple light sources. In this implementation, the color of fluorescent excitation and emission is controlled by a pair of filters that can be configured and exchanged. Charged coupled device (CCD) or CMOS cameras are a popular detector for the capture of images, as their high frame

capture rates can provide basic imaging processing capabilities, including still images and motion video.

Epifluorescent microscopes provide a variable particle resolution depending on emission wavelength, the numerical aperture of the objective lens, and the refractive index of the medium between the objective and the target. For the emission of blue light, under optimal conditions, the minimum particle resolution size is approximately 250 nm[1]. Under this limit, groups of particles may blend into a single point, or become a diffuse cloud of intensity that may not be detected.

Although a common instrument, a lone epifluorescent microscope is an unreliable choice for low level detection of a variety of particulates, including HMW DNA, cellular debris, and drug delivery nanoparticles. The resolution limit may be too high to provide adequate particle counting and detection, and the CCD/CMOS detector may generate too much noise or loss in captured images.

Scanning confocal microscopes[8] (Figure 2) improve upon the basic epifluorescent microscope by illuminating and imaging single points or lines and reconstructing a full image using processing software. Two pinhole apertures are placed after the illumination source and before the detector to eliminate out-of-focus light and improve resolution. A mechanically controlled mirror system is placed in line with the objective to optically scan a desired area and collect data on a point-by-point basis.
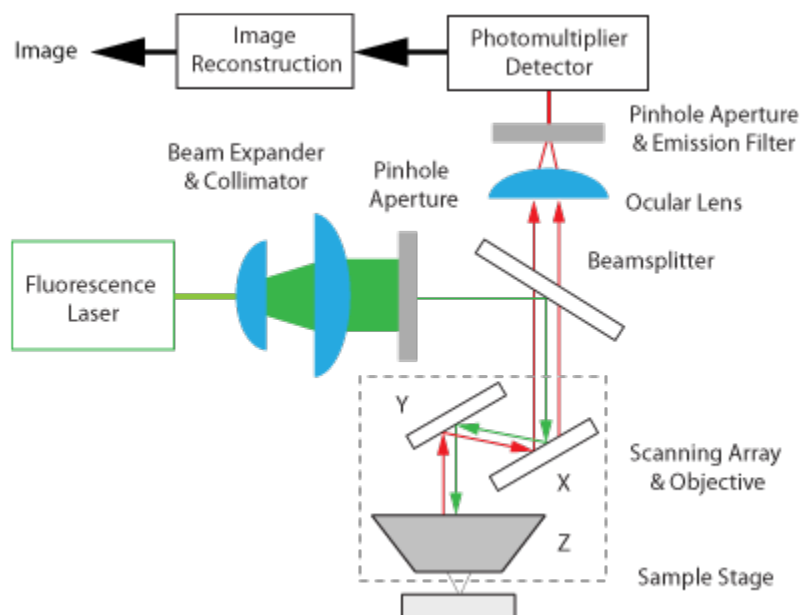
Figure 2: Point Scanning Confocal Microscope System. Shown system is configured for reflectance imaging with laser illumination and a photomultiplier detector.

Since points are individually captured, the detector can be changed from a pixilated CCD to a photomultiplier or avalanche photodiode, both of which have the capability to detect a single emitted photon. Rather than using an arc lamp, confocal microscopes generally employ single-wavelength sources such as a laser or a high quality LED to maximize the intensity at a desired excitation.

Confocal microscopes provide far greater sensitivity and resolution than a wide field microscope; a single 200 nm particle may be resolved by this system[1]. These improved aspects make it a better choice for low level nanoparticle detection, but come at a price. Since an individual image must be reconstructed from individual points, capture rates may be slow (preventing live capture of time lapse images or movies), and supporting software is required[2].

The most drastic difference between the two systems is cost. A common epifluorescent microscope is between \$30,000 and \$40,000 USD[2]. Confocal microscopes, being a more complex and specialized device, carry a significantly higher cost. Depending on the illumination sources and processing required, a single confocal microscope system may be priced at or above \$300,000 USD[2], almost ten times higher than an epifluorescent system.

Although a confocal microscope system is an ideal choice for low level nanoparticle detection, its prohibitive cost is an enormous issue that has limited its proliferation into general laboratory settings. A detection diagnostic for drug delivery nanoparticles, for example, would need to carry a low enough price for general clinics to purchase.

Instead of swapping to a more expensive imaging system, enhancing the basic epifluorescent microscope is also an option. Replacing a standard CCD for an EM-CCD (electron multiplied CCD) will provide additional sensitivity, but may add \$20-30,000 USD in cost and lead to the cost issue raised previously. Rather than focusing on changes to the detection system itself, changing the presentation of the sample may prove to be more efficient. Mainstream biology, for instance, employs a number of sample preparation methods that can potentially be applied to improve system performance and visibility.

2.2 Dielectrophoresis

Electrokinetic processes, the movement of particles in an applied electric field, are frequently used in the analysis of biological samples when fluidic driven options are undesirable. The most common of these is DC electrophoresis, which induces the

movement of molecules and particulates by net charge[6]. Combining different hydrogels with electrophoresis provides a number of different modes of particle separation and concentration, including charge to mass ratio and molecular weight. Particles with no net charge do not normally experience movement under a uniform electric field, which limits the application of electrophoresis to neutral particles such as whole cells and viruses.

Dielectrophoresis, a close relative of DC electrophoresis, is an electrokinetic force that is generated on microscopic particles suspended within a non-uniform electric field[6,7]. If a direction or intensity gradient exists along a set of electric field lines, an induced dipole moment will form inside and along the surface of a dielectric particle. Depending on the relationship between a particle and the medium it is suspended in, it will either move towards, or be pushed away from, regions of high electric field. DEP functions in both DC and AC electric fields as long as the field lines are non-uniform.

Unlike DC electrophoresis, which is limited to the separation of charged particles, DEP has the distinction of being able to separate, concentrate, and trap particles by a variety of properties including size, conductivity, density, polarizability, permittivity, and charge. Since DEP functions using an induced rather than intrinsic dipole, it can be used with both electrically charged and electrically neutral particles. The force generated through DEP is defined as[6]:

$$F_{DEP} = 2\pi r^3 \, \epsilon_m \, Re\{K(\omega)\} \, \nabla E^2$$

The magnitude of the DEP force is linearly dependant on a combination of four variables: the particle volume, the polarity/permittivity of the medium, the real part of the Clausius-Mossotti Factor (K(ω), see 2.2.1), and the gradient of the squared electric field,

also known as the field gradient factor. For an alternating electric field, the root mean square value is used to calculate the induced force.

2.2.1 Clausius-Mossotti Factor

The frequency response and force direction of particles under DEP is governed by the Clausius-Mossotti Factor, which represents the interaction between the particle and the medium it is suspended in. For spherical particles, the CM Factor is defined as $K(\omega)$ below[6]. The complex dielectric constant (ϵ^*) is defined as the arithmetic combination of bulk permittivity (ϵ) and a frequency dependant conductivity (σ).

$$K(\omega) = \frac{\epsilon_p^* - \epsilon_m^*}{\epsilon_p^* + 2\epsilon_m^*}$$

$$\epsilon^* = \epsilon_r \epsilon_0 + \frac{\sigma}{j\omega}$$

A positive CM Factor indicates that the DEP force will be defined in parallel with the field gradient factor, driving particles towards areas of high electric field; this is defined as positive DEP. If the CM Factor is negative, the opposite is true, and particles move towards areas of low electric field; this is defined as negative DEP. For spherical particles, the CM Factor may range between -0.5 and 1. As a result, the trapping force on a particle under positive DEP is generally higher than the force on a particle under negative DEP[7]. At low frequencies, the particle and medium conductivity terms dominate the CM Factor, causing separation and trapping to be primarily performed by differences in conductivity. At high frequencies, the permittivity term dominates; most

dielectric particles in a highly polar medium, such as water, will experience negative DEP in this region[6].

Figure 3 shows a plot of the CM Factor for a set of two polystyrene nanoparticles and two cells suspended in 1x TBE buffer, which has a fluid conductivity of 110 mS/m. The 40 nm PS nanoparticles are coated with a semiconducting outer layer that causes them to experience positive DEP at low frequencies due to a higher surface conductance than the surrounding medium[6]. These particles serve as an appropriate approximation for a number of other nanoparticulates, including DNA and viruses. The 10 um PS nanoparticles are uncoated, leaving a strong insulating interface with the water; as a result, they experience negative DEP over all frequencies[6].

The behavior of the two cells, a human blood cell[6,9] and an E.Coli bacterium[6,10], is governed by not only the interaction of the cell with the medium, but also the interactions of the internal layers. The red blood cell has an insulating membrane that is selectively polarizable during a window of frequencies centered at 1 MHz. The bacterium experiences weak positive DEP at low frequencies due to a semiconducting cell wall and strong positive DEP during a window in which the membrane can be strongly polarized.

All of the particles experience negative DEP at high frequencies, as their dielectric constants are all lower than that of the medium.
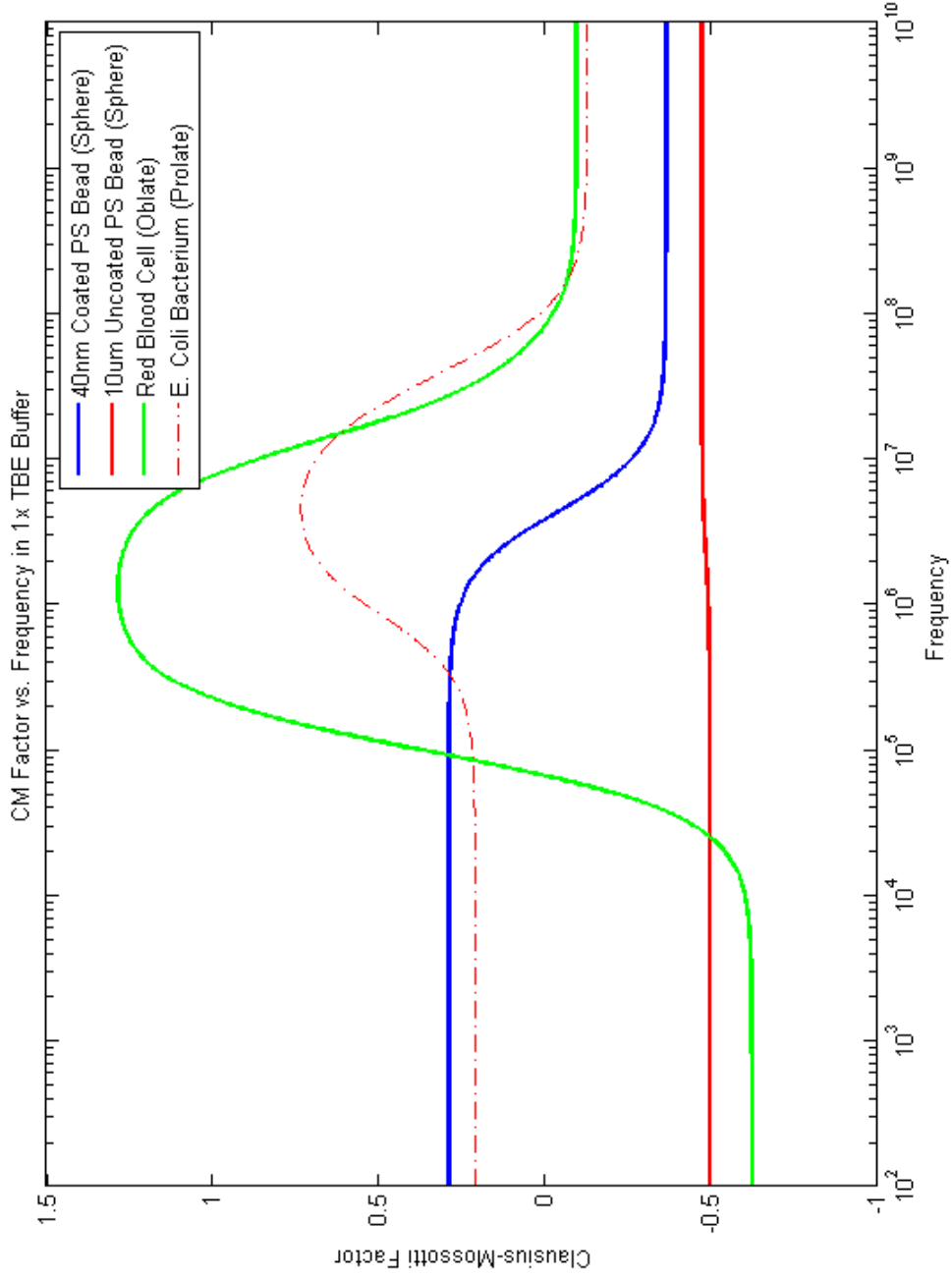
Figure 3: Plot of the Clausius-Mossotti Factor. Example plots included for 40 nm Carboxylate Coated PS Nanoparticles (Spherical 3-Layer)[6] , 10 um Uncoated PS Nanoparticles (Spherical 1-Layer)[6] , a Human Red Blood Cell (Oblate 2-Layer)[6,9] , and a Gram Negative E.Coli Bacterium (Prolate 4-Layer)[6,10]

2.2.2. Minimum Particle Size over Brownian Motion

A major factor in the effectiveness of the dielectrophoretic force is the size of a specific particle; as the volume decreases, the dipole force generated will decrease at the same rate. For extremely small particulates such as HMW DNA fragments, viruses, or cellular organelles, effective separation and trapping may cease to exist below a certain size. At this limit, Brownian motion and random thermal drift will nullify any induced force. The minimum particle size for effective trapping has been previously calculated by Hughes[7] and is given by:

$$r > \sqrt[3]{\frac{10\ k_b\ T}{\pi\ \epsilon_m\ Re\{K(\omega)\}\ \Delta d\ \nabla E^2}}$$

For a fixed temperature T and a medium ε, the minimum radius is inversely proportional to the Clausius-Mossotti Factor, the width of the trap Δd, and the field gradient factor. For a pair of electrodes, the trap width can be defined as the shortest gap between the anode and cathode.

2.2.3 Dielectrophoresis of Layered Spherical Particles

The base description of the Clausius-Mossotti Factor only describes the behavior of a single homogeneous particle and does not account for multiple layers. Coated drug delivery nanoparticles, for example, may have a fluidic interior surrounded by a thin membrane and a hard protein shell. If spherical symmetry holds, an effective medium theory can be applied to compensate for multiple internal layers. Two separate layers can combined into a single effective layer through the following relation[6]:

$$\epsilon_{eff,i}^{*} = \epsilon_i^{*} * \left[\frac{a^3 + 2\left(\dfrac{\epsilon_{i-1}^{*} - \epsilon_i^{*}}{\epsilon_{i-1}^{*} + 2\epsilon_i^{*}}\right)}{a^3 - \left(\dfrac{\epsilon_{i-1}^{*} - \epsilon_i^{*}}{\epsilon_{i-1}^{*} + 2\epsilon_i^{*}}\right)} \right]; \quad a = \left(\frac{r_i}{r_{i-1}}\right)$$

If a particle is composed of more than two layers, an effective complex permittivity is calculated for the two inner most layers first; this value is then used to calculate another effective complex permittivity in tandem with the third layer. This process may continue iteratively until each particle layer is used. The final effective complex permittivity can be placed in the original Clausius-Mossotti Factor formula.

2.2.4 Dielectrophoresis of Elliptical Particles

The base Clausius-Mossotti factor provides an adequate model for spherical particles, but does not give a valid result for ellipsoidal shapes. Red blood cells (oblate ellipsoid) and E.Coli bacteria (prolate ellipsoid) are two important biological examples of this symmetry. For particles of these shapes, the CM Factor takes a general form of[10]:

$$K_x(\omega) = \frac{1}{3}\left[\frac{\epsilon_{i-1}^{*} - \epsilon_i^{*}}{\epsilon_i^{*} + A_x(\epsilon_{i-1}^{*} - \epsilon_i^{*})} \right]$$

Unlike the spherical case, the elliptical distribution includes an additional term, A, which represents the depolarization factor of the ellipsoid across one of its axes. The formula for A differs based upon the symmetry of the ellipsoid, with prolate (a > b = c) and oblate (a = b > c) varieties being the most common. The CM factor for each axis (x,y,z) must be calculated individually and then summed together to provide the full value. As a result, the magnitude of the CM factor may fall below -0.5 or above 1

depending on differences in polarizability between the individual axes of rotation. Due to asymmetry, the effective medium theory cannot be used to approximate ellipsoidal particles with multiple layers. Instead, the CM factor of each layer must be calculated iteratively.

Chapter 3: Experimental Procedure

3.1 Materials

The analytical system used for experimentation is a combination of a standard epifluorescent microscope and a 100-site microelectrode array powered by a function generator.

3.1.1 Microscope System

The microscope employed for the research is an Olympus BX41 upright epifluorescent microscope. The system uses a 100 watt mercury arc lamp for illumination and a 16-bit (per channel) 5-megapixel RGB Bayer filter CCD camera for detection. Emission and excitation filters for Texas Red (650 nm) and FITC (520 nm) were used to generate fluorescence images, and a set of two neutral density filters were used to control illumination intensity. The included Olympus software provides basic image processing capability, most notably the ability to integrate images into exposure times up to 60 seconds in length. The approximate retail cost for the complete microscope system is $35,000 USD.

Table 1: Resolution Limits of the Olympus BX41 Microscope.

Objective	NA	Res. Limit at 520 nm	Res. Limit at 650 nm
4x	0.13	2400	3000
10x	0.3	1040	1300
50x	0.5	624	780

The objectives included with the microscope are configured for long working distances and have very low numerical apertures. The long focus distance is required to successfully image the microelectrode array through its supporting microfluidic cartridge.

High NA epifluorescent microscopes using fluid immersion are capable of sub-300 nm resolution limits, but this is not the case here. For green and red particles, the resolution limit of the 10x objective is 1040 nm and 1300 nm, respectively[1]. It is important to note that this *does not prevent detection* of particles smaller than these values, but will interfere with particle counts. For example, if two 100 nm nanoparticles are less than 1000 nm apart (for green fluorescence), they will not be individually seen and will instead merge into a single spot.

Optical imaging has three tradeoffs that commonly come into play: sensitivity, specificity, and speed. The fluorescence imaging performed in this project involves the detection of particles suspended in a fluid medium. Buoyancy and gravity generally offset each other for particles with a density close to that of the fluid, leaving them to drift randomly under Brownian motion[7]. To properly resolve individual particles, this movement requires the sample to be viewed with a short imaging time. A short imaging time is generally used in tandem with high illumination intensity in order to reach the level of sensitivity required by the detector.

The use of high illumination intensity brings number of undesirable side effects, including heating and photobleaching. For biological samples that may be partially damaged by high energy photons, these become even more significant. If samples can be effectively immobilized, a low intensity and long exposure image becomes a more attractive and gentle option. If immobilization is impossible and high intensity is undesirable, the resolution of details in an image will be lost and a bulk fluorescence image will be generated.

3.1.2 Microelectrode Array & Power Source

The interrogation of fluid media with suspended nanoparticulates has been completed using the Nanochip 100, a 100-site individually addressable microelectrode array produced by Nanogen, Inc. (Figure 4). The array is made of a 10x10 grid of circular electrodes, each having a diameter of 80 micrometers, and spaced apart at a pitch of 200 micrometers (center-to-center)[3]. A microfluidic chamber is mounted surrounding the chip, holding a volume of approximately 20 microliters.
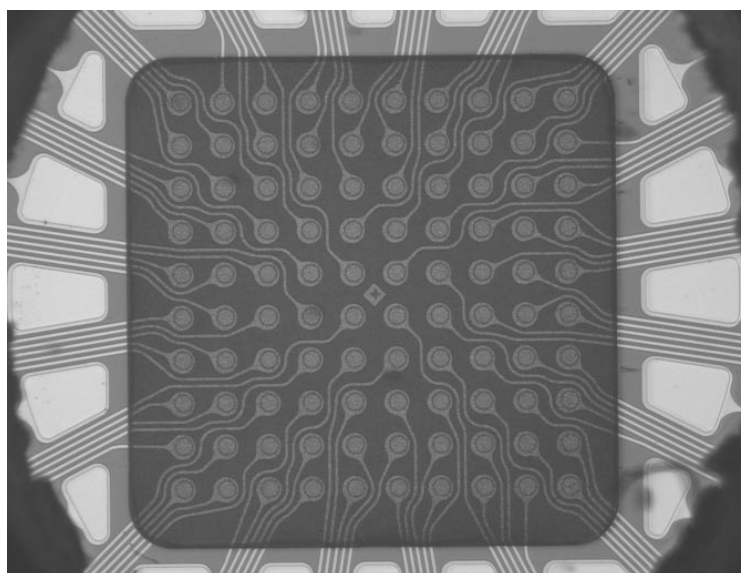
Figure 4: Surface of the Nanochip 100.

The electrode array is composed of vapor-deposited platinum electrodes on a silicon base wafer with an insulating coating of silicon dioxide (Figure 5)[4]. To protect analytes in solution from electrochemical effects at the surface of the chip, the array is coated with a layer of polyacrylamide hydrogel. Unfortunately, the high level of surface area in the hydrogel layer also introduces significant non-specific binding. Particulates may end up attaching or becoming embedded in the hydrogel through random drift.

Thermoelectric Fluid Flow
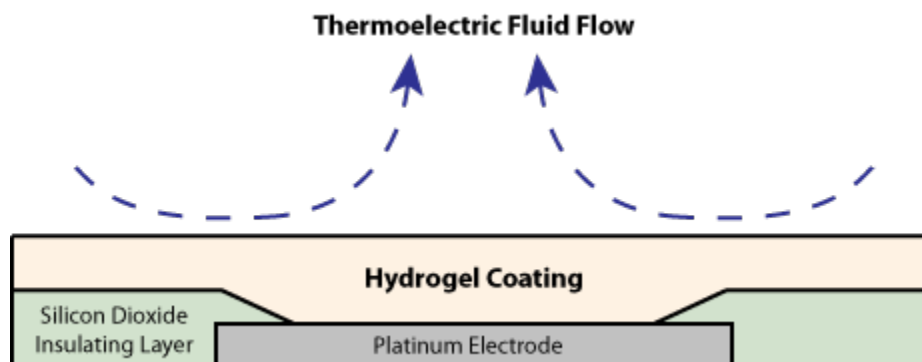
Figure 5: Side View of Single Microelectrode. The diameter of the opening above the platinum electrode is fixed at 80 micrometers and insulated by a layer of Silicon Dioxide. The direction of the induced thermoelectric fluid flow is also indicated by blue arrows.

The electrode array is powered by an Agilent 33250A function generator, capable of operation up to 80 MHz and a 20V peak-to-peak voltage when using a high impedance load. The current output is limited to 100 mA, which limits the number of maximum electrodes that may be operated at any one time. Each set of opposing electrodes serves as a miniature parallel circuit, increasing the current consumption of the array. If the current requirement is too high, the system will be unable to reach a desired voltage and the strength of the DEP force will be reduced accordingly.

The combined cost of the Nanochip 100 and Agilent function generator is $4,700 USD, bringing the complete analytical system cost to approximately $40,000 USD. Waveform generators powered by less precise electronic components, such as a Syscomp WGM-201 ($227 USD), are considerably cheaper and can reduce the system cost considerably. In either case, the total cost is less than one fifth that of a scanning confocal microscope system ($300,000)[2].

3.1.3 Induced Fluid Flow

When the microelectrode array is active, current flowing through the fluid medium will induce localized joule heating above each individual electrode. As the heated fluid rises, cooler fluids from the interelectrode gaps will move replace it. This creates an electrothermal convective fluid flow (Figure 5) that may overpower any dielectrophoretic force exerted on individual particles[7,17]. This effect decreases with an increase in applied frequency. Applied voltages on the chip must remain low enough to prevent overheating and localized boiling of the fluid, or to limit the speed of the electrothermal flow. Other sources of fluid flow, including electroosmosis, are extant but too weak to significantly interfere with dielectrophoretic collection[7].

3.2 Method of Operation

All of the experiments run using the microelectrode array follow the same basic procedure. The steps are as follows:

1. Insert target analyte into a buffer or carrier solution. If required, label target with an applicable fluorophore (ex. DNA labeled with SYBR Green).

2. Insert buffer with target analyte into the microelectrode fluid chamber. Configure the frequency and voltage of the power source to allow for positive DEP of the target analyte, and activate for a set period of time.

3. If necessary, use a fluidic wash to remove unwanted debris, while leaving the electric field active. A fluorescent image of the array is taken afterwards and compared to a before image or a control.

Chapter 4: Experimental Results

An important clinical detection level is 10 ng of analyte per milliliter of fluid; this corresponds to the normal level of DNA that exists in the blood of a healthy human individual[11]. Elevated levels of DNA, particularly of the high molecular weight variety, have the potential to be used as a major diagnostic tool for infectious disease, physical injury, and cancer. For the combined microelectrode array and epifluorescent microscope analytical system, 10 ng/mL will serve as the major detection goal for nanoparticulates.

The experiments performed are as follows:

1. Baseline Bulk Detection Limit of Microscope

2. Simulations of the Microelectrode Array

3. Concentration of Fluorescent Nanobeads in Buffer Solution

4. Concentration of Fluorescent Nanobeads from Red Blood Cells in Buffer Solution

5. Concentration of DNA from Whole Blood

4.1 Bulk Detection Capability of the Epifluorescent Microscope

To establish the baseline detection capability of the analytical system, a serial dilution of 100 nm diameter red fluorescent carboxylate-modified polystyrene nanobeads (Invitrogen) and 20 nm diameter green fluorescent carboxylate-modified polystyrene nanobeads (Invitrogen) were prepared in 0.1x TBE buffer (10 mS/m) (Fisher). Mass concentrations ranged between 100 ug/mL and 1 ng/mL in magnitudes of 10. 65 uL of each solution was placed inside of a single well in a black fluorometer plate (Nunc) and imaged through the microscope. As the particles in solution are free to move and below

the resolution limit of the microscope, the resulting image corresponds to a bulk fluorescence value for the entire fluid medium.

To maintain equal peak image intensity, the exposure time for decreasing concentrations was increased gradually from 1 second to 30 seconds. The intensity across each image was statistically analyzed, with the mean and mode values extracted for comparison. The collected values for images with exposure times above 1 second have been divided to normalize them to a 1 second scale.
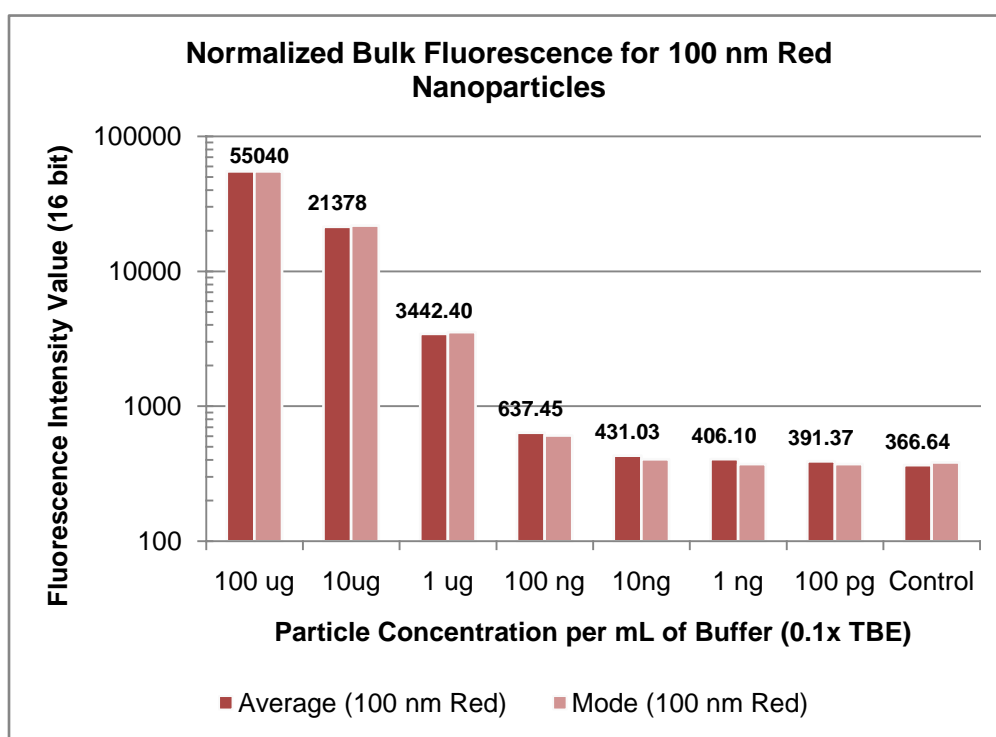
Figure 6: Bulk Fluorescence Values for 100 nm Red Fluorescent PS Nanobeads. Particles have been suspended in 0.1x TBE buffer; all intensity values are normalized to a 1s exposure time.

Analysis of the bulk fluorescence images indicates that the Olympus microscope loses the capability to reliably distinguish fluorescence levels below a nanoparticle concentration of 1 ug/mL, approximately 100 times higher than the intended goal (10 ng/mL). The red (Figure 6) and green (Figure 7) fluorescent nanoparticles both begin to

drop off at the same concentration, indicating that their behavior is approximately equal.
It is important to note that at an individual mass concentration, there are approximately
120 times more 20 nm nanobeads than 100 nm nanobeads (Table 2); this difference
does not seem to change the detection limit of the bulk fluid.
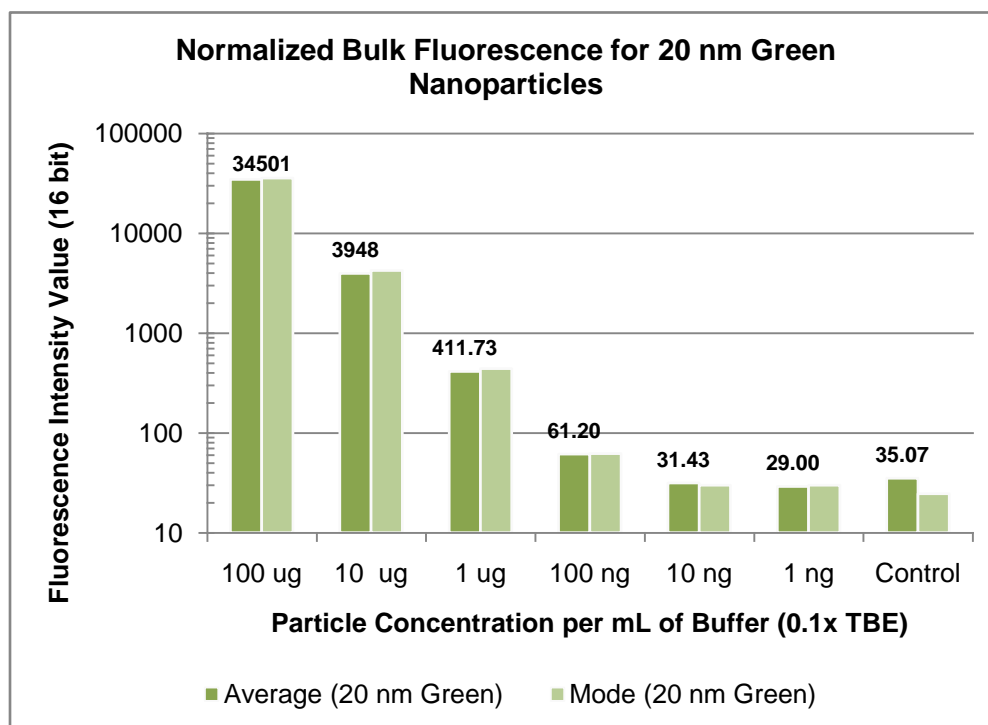
Figure 7: Bulk Fluorescence Values for 20 nm Green Fluorescent PS Nanobeads. Particles have
been suspended in 0.1x TBE buffer; all intensity values are normalized to a 1s exposure time.

Bulk fluorescence is commonly detected using a fluorometer, a specialized
instrument that contains a variable wavelength filter that can be configured to any pair of
excitation and emission wavelengths. The same nanoparticle dilutions used to establish
the microscope's bulk fluorescence were subsequently analyzed with a Tecan
fluorometer. As the fluorometer is specifically designed for quantitative bulk fluorescent
detection rather than the generation of an image, it provides a reliable comparison to
establish the capability of the microscope.
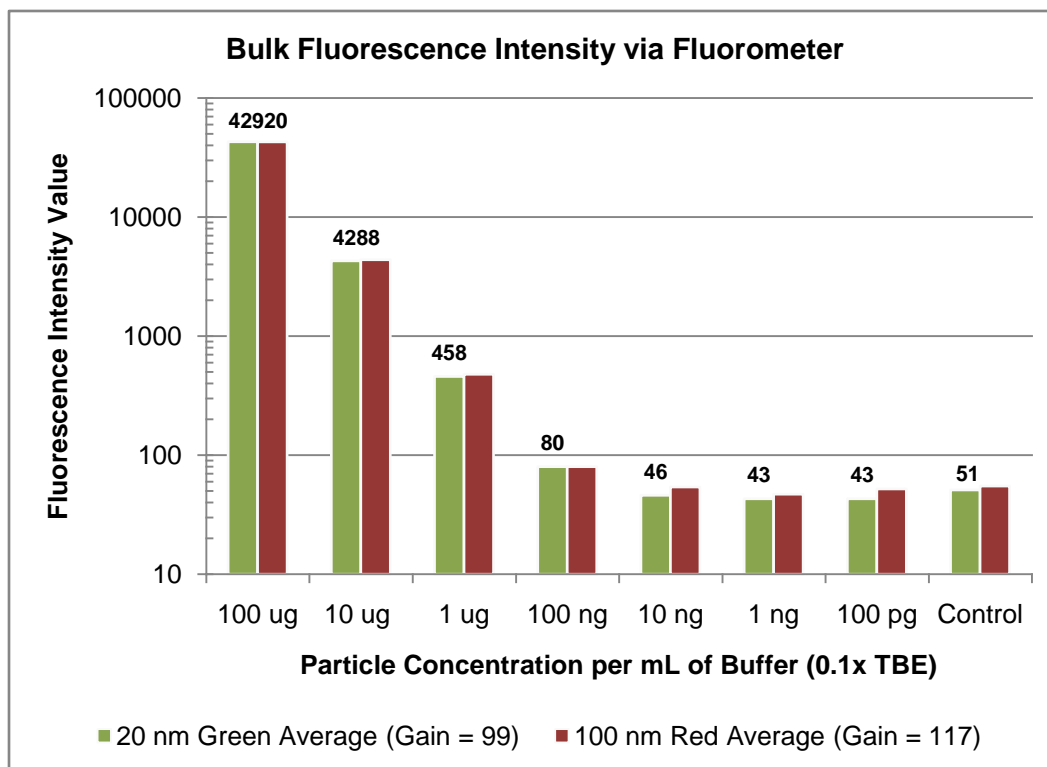
Figure 8: Bulk Fluorescence of Nanobeads via Tecan Fluorometer. Analysis of both 20 nm green and 100 nm red nanoparticles are included.

The quantitative values calculated by the fluorometer (Figure 8) indicate a logarithmic drop in fluorescence from 100 ug/mL to 1 ug/mL, in line with the 10x serial dilution curve. The logarithmic decrease halts at 100 ng/mL, and any concentrations below this level become indistinguishable. At this point, the volume of fluorescent material becomes too small to detect. The detection capability of the fluorometer is a close match to that of the lone microscope; particle counts under 1 ug/mL become unreliable on both instruments.

Table 2: Nanoparticle Counts Per Dilution. Numbers included for a full milliliter, the microelectrode chamber, and the approximate count on a 3x3 electrode array.

Mass/mL	Number in 1 mL		
	100 nm	40 nm	20 nm
1 ug	1.82E+09	2.84E+10	2.27E+11
100 ng	1.82E+08	2.84E+09	2.27E+10
10 ng	1.82E+07	2.84E+08	2.27E+09
1 ng	1.82E+06	2.84E+07	2.27E+08
100 pg	1.82E+05	2.84E+06	2.27E+07
10 pg	1.82E+04	2.84E+05	2.27E+06

Mass/mL	Number in 20 uL (Full Chamber)		
	100 nm	40 nm	20 nm
1 ug	3.64E+07	5.68E+08	4.55E+09
100 ng	3.64E+06	5.68E+07	4.55E+08
10 ng	3.64E+05	5.68E+06	4.55E+07
1 ng	3.64E+04	5.68E+05	4.55E+06
100 pg	3637.83	56841.10	4.55E+05
10 pg	363.78	5684.11	45472.88

Mass/mL	Number on 9 Electrodes (9%)		
	100 nm	40 nm	20 nm
1 ug	3.27E+06	5.12E+07	4.09E+08
100 ng	3.27E+05	5.12E+06	4.09E+07
10 ng	32740.47	5.12E+05	4.09E+06
1 ng	3274.05	51156.99	4.09E+05
100 pg	327.40	5115.70	40925.59
10 pg	32.74	511.57	4092.56

4.2 Array Configuration & Simulations

By combining the concentration, trapping, and separation capability of dielectrophoresis with the base imaging capability of the epifluorescent microscope, it may be possible to reach the 10 ng/mL clinical detection limit. Due to the low relative cost of the combined power source and microelectrode array, it would be accomplished without the addition of expensive optical components to the microscope. The need to

change to a different detection platform, such as a confocal microscope, would also be avoided. The effects of voltage, medium conductivity, and frequency on dielectrophoresis have been previously discussed; the geometric configuration of the microelectrode array and its physical implications must also be considered.

4.2.1   Electrode Configurations

The Nanochip 100 microelectrode array is individually addressable, allowing each electrode to be configured to either polarity. An endless number of possible geometric configurations are possible when performing dielectrophoretic separation and concentration. Two have been selected for experimental investigation: an alternating checkerboard and a box. Due to current limitations with the selected power source (Agilent function generator), the experiments are limited to a 3x3 active array at a single time so that maximum voltage and dielectrophoretic force are maintained.

4.2.2   Checkerboard Configuration
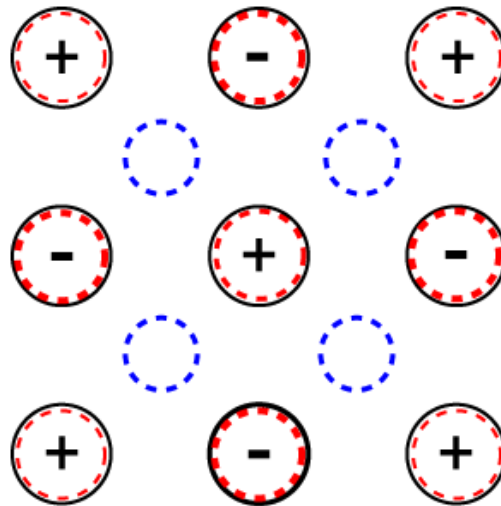
Figure 9: 3x3 Checkerboard Configuration. Adjacent electrodes have alternating polarities, as noted by the plus and minus signs. Positive DEP traps are highlighted in red and negative DEP traps are highlighted in blue.

A checkerboard pattern has been used in prior research[3] for the separation of nanoparticles and DNA from low and high conductance buffers. Adjacent electrodes are set to alternating polarities, creating a total of 9 high field trapping zones (red) at the edge of each electrode and 4 low field trapping zones (blue) in between. In a 3x3 array, the sets of anodes and cathodes are not equal in number, creating an asymmetry in fluid flow, electric field intensity, and current density. The set of 4 common electrodes will experience a slightly stronger high field trap, enhancing their collection efficiency over the other 5. This effect is most easily seen when using high conductance fluids. The checkerboard configuration is extremely powerful for separation purposes due to strongly defined positive and negative trapping regions.

4.2.3   Box Configuration
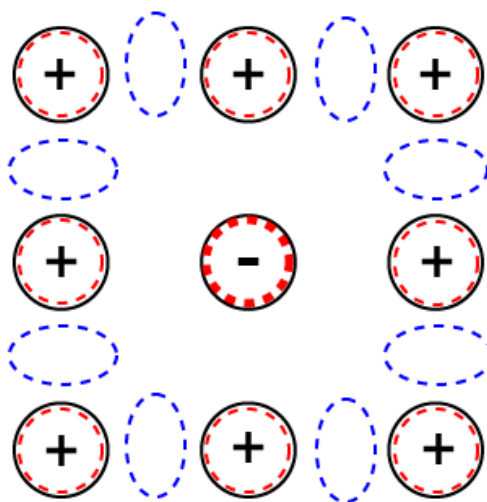
Figure 10: 3x3 Box Configuration. Electrode polarities noted by plus and minus signs; positive and negative traps noted by red and blue lines, respectively.

An additional 3x3 array configuration that has been explored is a box or ring configuration, where the center electrode is opposed by the eight surrounding

electrodes. Unlike the checkerboard, there is a very strong high field collection point at the center, and a set of weaker low field collection zones between the outer electrodes. The outer electrodes have the capability to induce positive DEP collection, but the field strength is significantly weaker than the center. Theoretically, this configuration is better suited for positive DEP concentration and trapping due to the strong high electric field at the center; the tradeoff is weaker separation from particulates under negative DEP.

4.2.4   Minimum Particle Trapping Size

As previously stated in section 2.2.2, a minimum particle trapping size exists for any individual combination of a field gradient factor (electric field gradient) and the opposing electrode gap[7]. The Nanochip 100 features 80 um diameter electrodes placed 200 um apart center-to-center. For both the checkerboard and box electrode configurations, the minimum electrode gap is 120 um; this value can be placed into the minimum size function and used to calculate the required field gradient factor for an individual particle size. A plot of this function is shown in Figure 11.

For the previously mentioned 20 nm and 100 nm polystyrene nanoparticles, the field gradient factor must have an intensity of at least 10^{16} and 10^{14} V^2/m^3, respectively, to overcome random Brownian motion. Larger particulates require less electric field intensity to induce net movement due to the volume dependence of the DEP force; a red blood cell (~10 um), for example, only requires a field gradient factor of 10^8 V^2/m^3. For nanoparticle separation, concentration, and trapping, the applied electric field must be high enough to overcome random drift in order to have the desired outcome.

Minimum Particle Separation Size for Electrodes with 120um Spacing
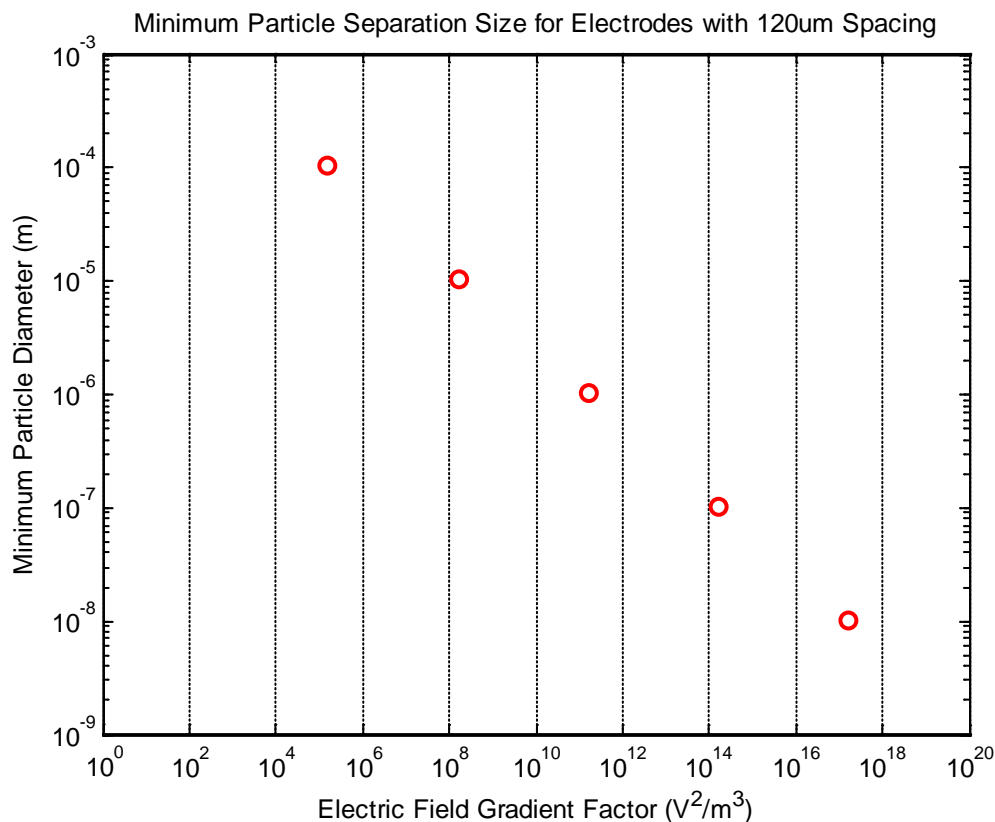
Figure 11: Minimum Particle Separation Size. Plot is configured for electrodes with 120 um spacing, and particles with a CM Factor of 1. Intersection points for particles of 100 um, 10 um, 1 um, 100 nm, and 10 nm are marked with red circles.

4.2.5   Physics Simulation of Checkerboard Configuration

To investigate the performance of the checkerboard array pattern, a number of physics simulations were performed using COMSOL Multiphysics (v4.0a) software. A three dimensional model of the 3x3 array was constructed utilizing a 200 um thick silicon wafer with 10 um thick copper electrodes and a 10 um thick insulating layer of silicon dioxide. A 400 um tall chamber of water was placed on top of the array with a conductivity of 110 mS/m, approximately equal to 1x TBE buffer. A voltage of 7.07 V_{RMS} (equivalent to 20 V_{PP}, the maximum voltage available with the Agilent function generator)

was used across the electrodes for all simulations. The base of the silicon wafer was set

to a temperature of 273 K (20 °C).
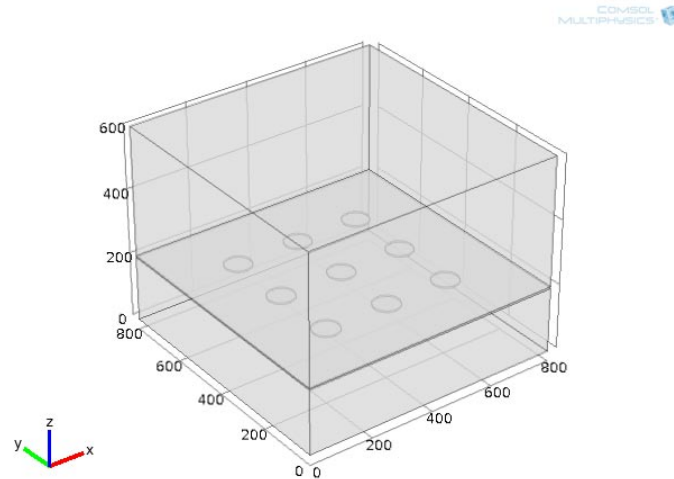
Figure 12: 3 Dimensional Model of 3x3 Array. Model drawn in COMSOL Multiphysics.

A three dimensional electric field model of the checkerboard is seen in Figure 13;

the slice in the xy plane is taken 5 um above the surface of the electrodes, while the yz

plane is taken halfway across the 3x3 array. The peak electric field on the checkerboard

pattern can be found on the set of four electrodes on the center of each side, with a

value of $2x10^5$ V/m. Similar to the diagram in Figure 9, the highest field regions are found

on the edge of each electrode, while the gap between four surrounding electrodes form

a distinct low field region. The high field regions (red) correspond to positive DEP

regions, while the low field regions (blue) correspond to negative DEP regions.

Figure 14 shows a top-down view of the electric field across the checkerboard

array and Figure 15 displays the current density seen 5 um above each electrode. Both

images illuminate an increased electric field and current flow through the outnumbered

set of electrodes. The current density, in particular, is of great importance: a higher level

of joule heating due to increased current will cause an elevated rate of thermoelectric &

convective fluid flow. At low rates convection may enhance DEP collection by slowly

circulating the fluid medium through the active DEP volume. At high rates the convection

may overpower and nullify any dielectrophoretic collection.
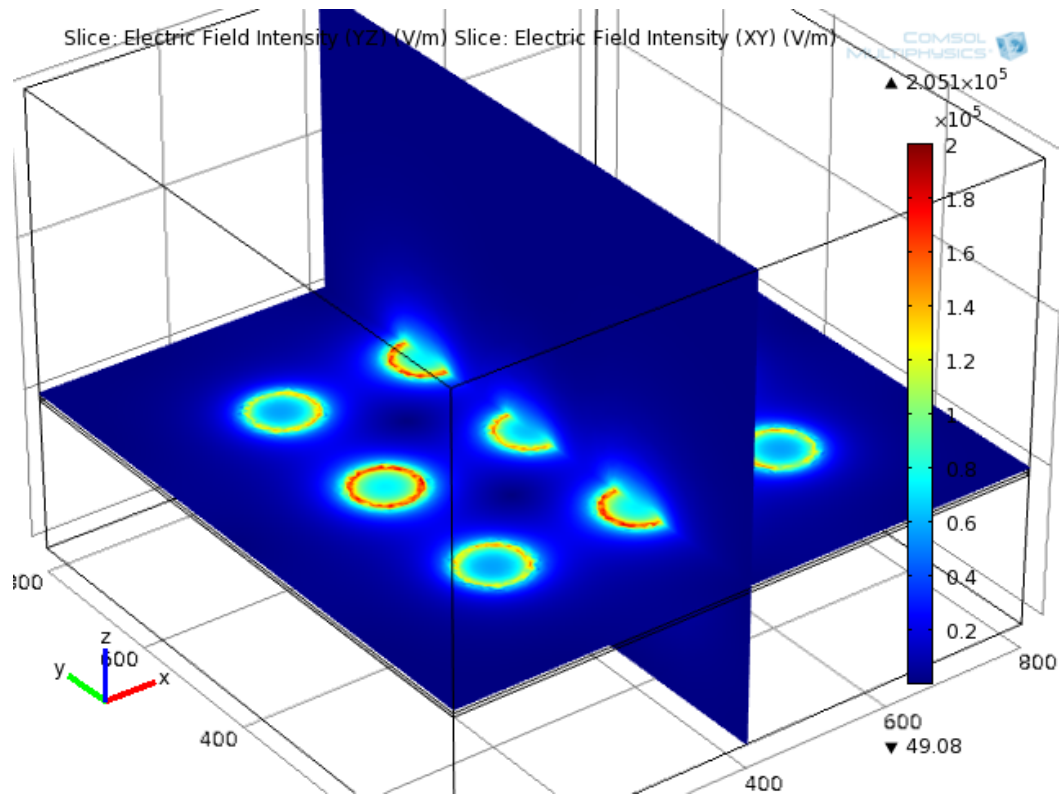
Figure 13: 3D Electric Field Model of the Checkerboard Pattern. Peak intensity (Red) corresponds to an electric field of $2x10^5$ V/m.
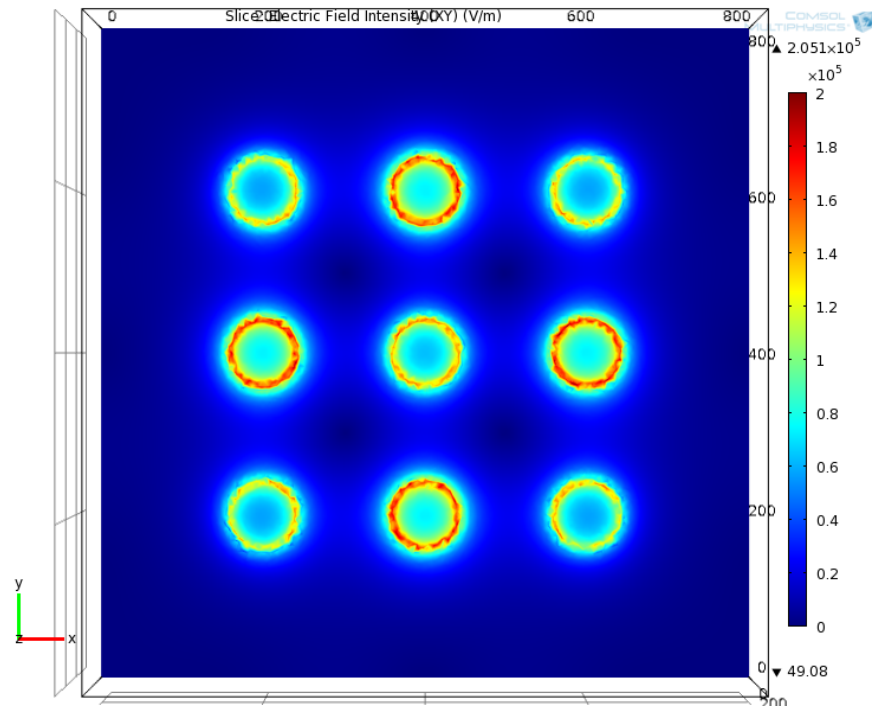
Figure 14: Electric Field Cross Section of Checkerboard Pattern. Plane of view is taken 10 microns above the electrode surface.
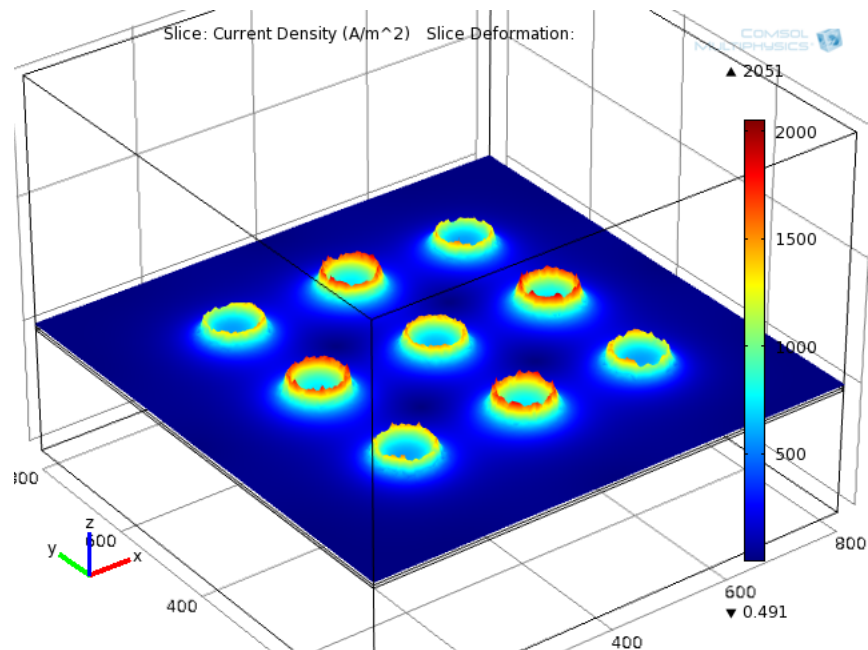
Figure 15: Current Density of Checkerboard Pattern. Peak value corresponds to a current density of 2000 A/m^2.

The field gradient factor (gradient of the squared electric field) has also been calculated using the COMSOL Multiphysics model. Using Figure 11 and the equation for minimum particle size in 2.2.2, a minimum intensity value can be calculated for trapping over Brownian motion. This can be used as a lower limit to determine the active DEP force volume for the array for a nanoparticle of a specific size. In Figure 16, a field gradient factor of 10^{14} is used as a minimum value, representing a nanoparticle of 100 nm with a CM factor equal to 1. Black areas in the plot represent "dead zones", where the magnitude of the DEP force is not high enough to overcome random drift.
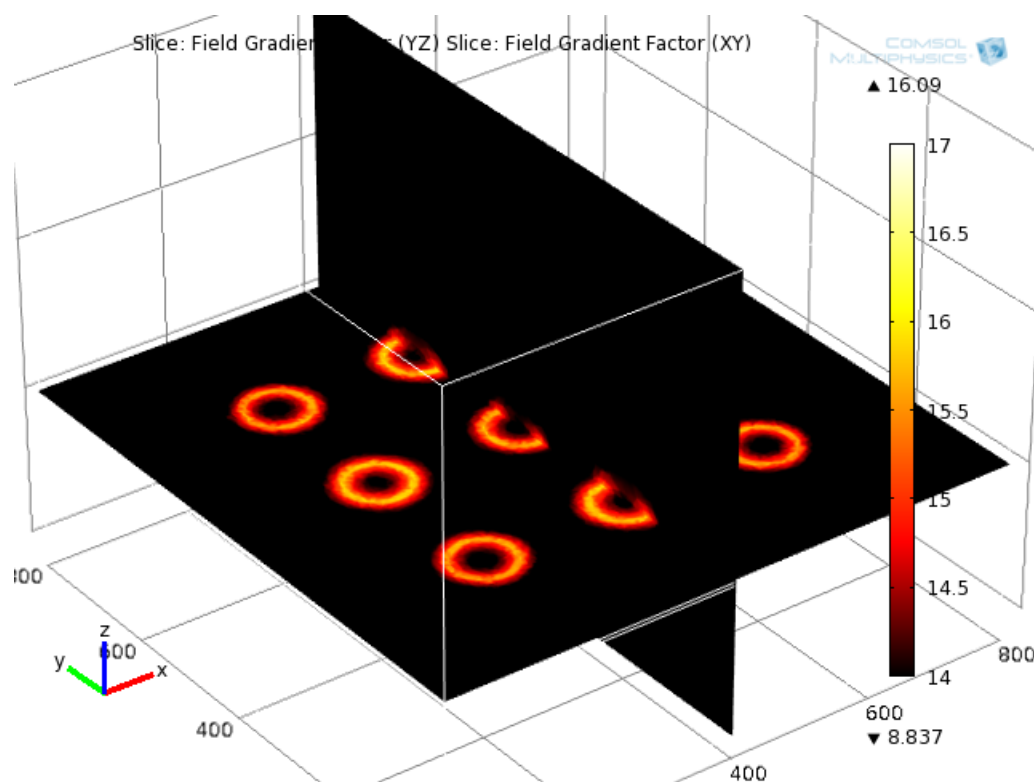
Figure 16: Field Gradient Factor of Checkerboard for 100 nm Particles. Intensity is plotted logarithmically. Areas in black fall below the minimum Field Gradient Factor for successful movement over Brownian motion.

The quantitative plot of the field gradient factor indicates that the active volume for a 100 nm particle is extremely small compared to the height of the fluid chamber; the active field only extends ~35 um upwards in the z-dimension. Along the surface of the chip, only areas close to the electrode edges have a high enough field gradient to induce a net dielectrophoretic force. An increase in the voltage used across the chip will increase the total active area, but limits on the available power supply and the capability of the Nanochip 100 prohibit this from being an option to improve efficiency during operation.

In comparison, Figure 17 shows the active DEP region for a particle with a radius of 10 um (CM Factor set to 1), which requires a field gradient of approximately 10^8. Unlike the plot for the 100 nm particle, the active volume for the 10 um particle encompasses the entire volume of the fluid chamber. Figure 18 shows an x-y slice 5 um above the electrodes with vectors representing the direction of the DEP force for a particle under positive DEP. As expected, the arrows are directed from regions of low electric field towards regions of high electric field. For a particle under negative DEP, the direction of the force will be inverted.
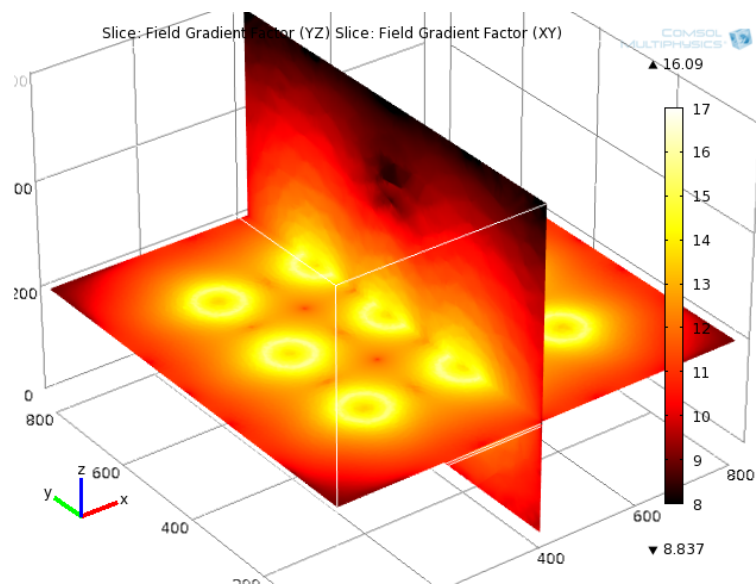
Figure 17: Field Gradient Factor of Checkerboard for 10 um Particles. Intensity is plotted logarithmically. Areas in black fall below the minimum Field Gradient Factor for successful movement over Brownian motion.
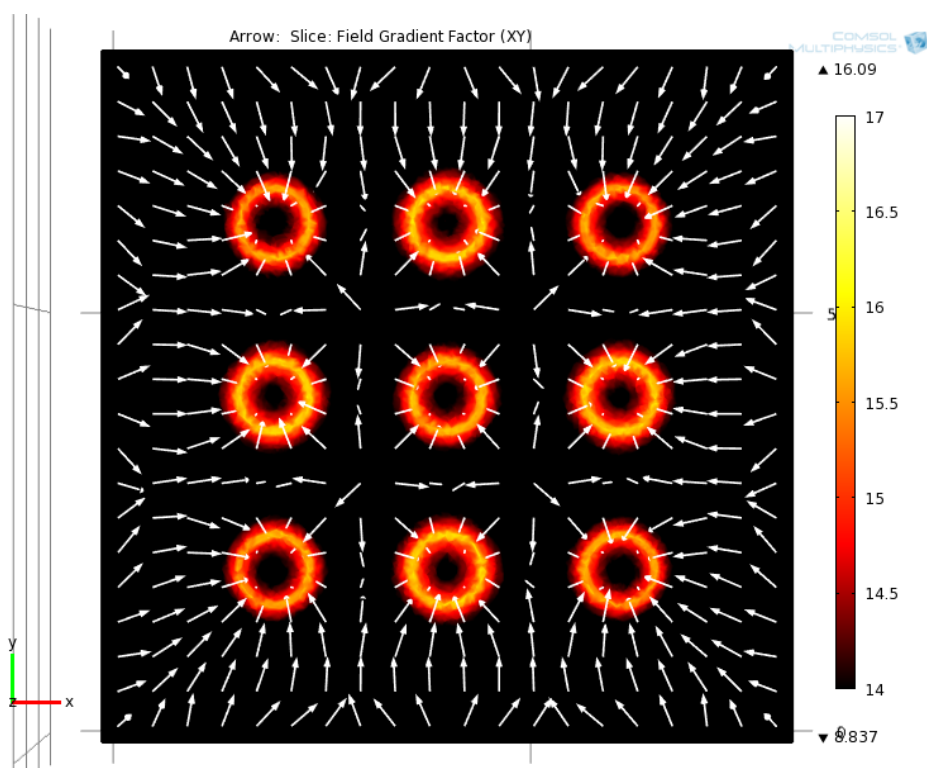
Figure 18: DEP Force Vectors for Checkerboard Array. Image taken 10 um above the surface of the electrodes for a particle size of 100 nm.

4.2.6   Physics Simulation of Box Configuration
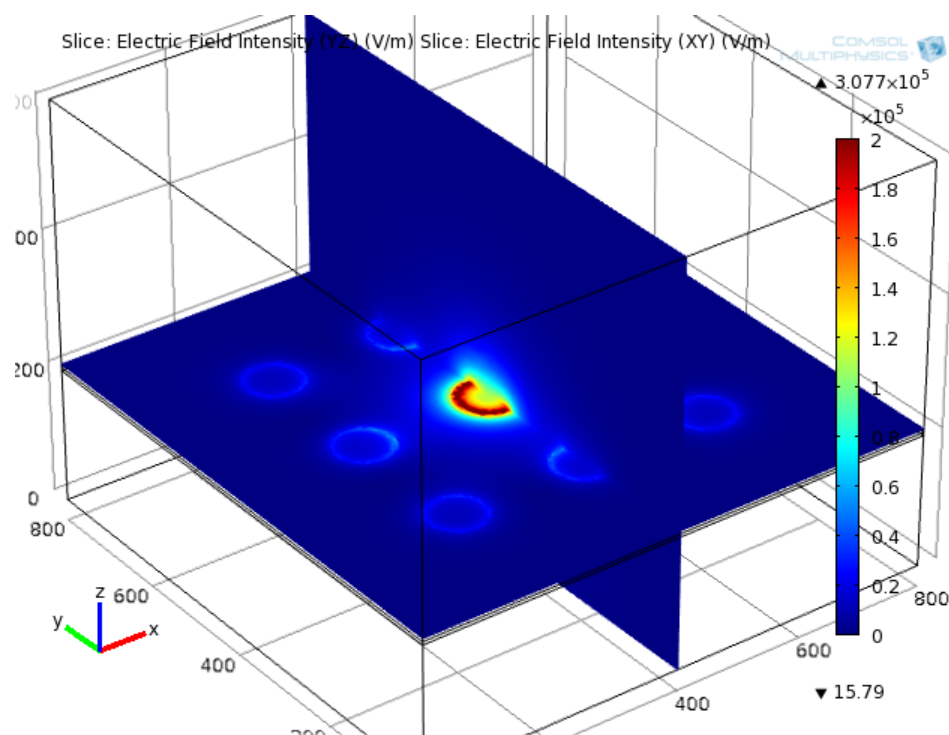
Figure 19: 3D Electric Field Model of the Box Pattern. Peak intensity (Red) corresponds to an electric field of $3x10^5$ V/m.

The box electrode configuration was simulated under the same conditions as the checkerboard model. This setup is expected to have a high electric intensity peak at the center electrode surrounded by a set of 8 weaker high field regions. An electric field simulation (Figure 19) indicates that the field intensity at the center is approximately 1.5 times higher than the peak intensity on the checkerboard pattern ($3x10^5$ vs. $2x10^5$). This should lead to a stronger high field concentration & trapping point at the center of the array compared to the outer ring and the checkerboard pattern.

For the detection of low levels of nanoparticulates and the enhancement of the epifluorescent microscope's capabilities, this electrode configuration may prove to be

more beneficial if the concentration capability at the center outperforms the

checkerboard. This, however, does not come without a price. Since all of the passable

current will be moving through the center electrode (Figure 20), the rate of thermoelectric

convection will be higher and is more likely to disrupt the dielectrophoretic force. The

applied voltage to the array may need to be reduced to prevent overheating, which will

also reduce the net DEP force on interrogated particles.
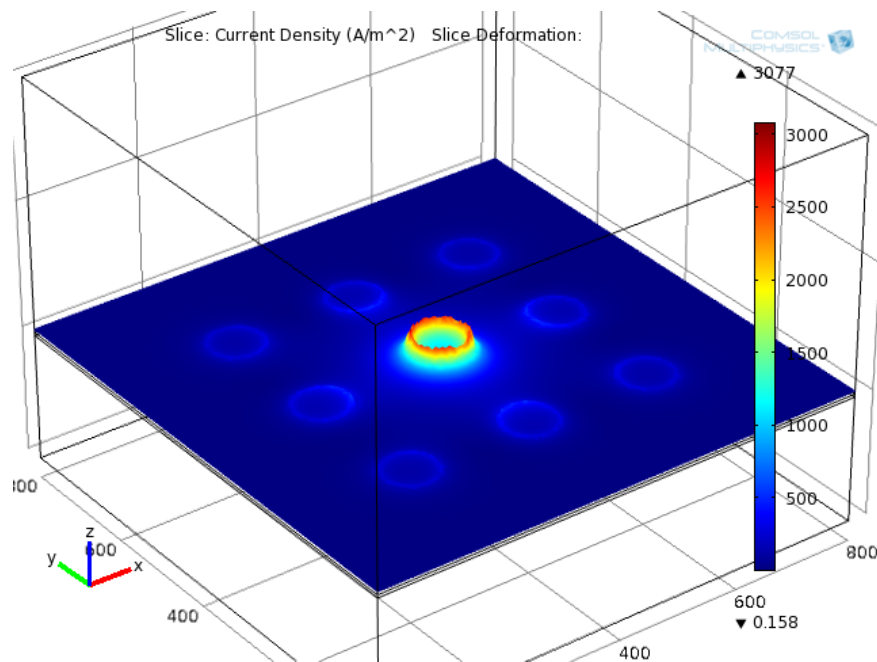
Figure 20: Current Density of Box Pattern. Peak value corresponds to a current density of 3000 A/m^2.

A plot of the field gradient factor was calculated for a 100 nm particle with a CM

Factor of 1 (Figure 21), similar to the checkerboard pattern in 4.2.5 (Figure 16). The

effective DEP field extends 50 um in the z-direction above the center point, an

approximately 50% increase in active volume. Along the surface of the chip, however,

the change in geometry reduces the active DEP area of the outer 8 electrodes by a

significant amount. The collection of nonresolvable particles at the center electrode will

be largely driven by a combination of the electrode's slightly larger active radius and the convective flow surrounding the middle of the array. For 100 nm particles, the force generated by the outer 8 electrodes is largely insignificant.
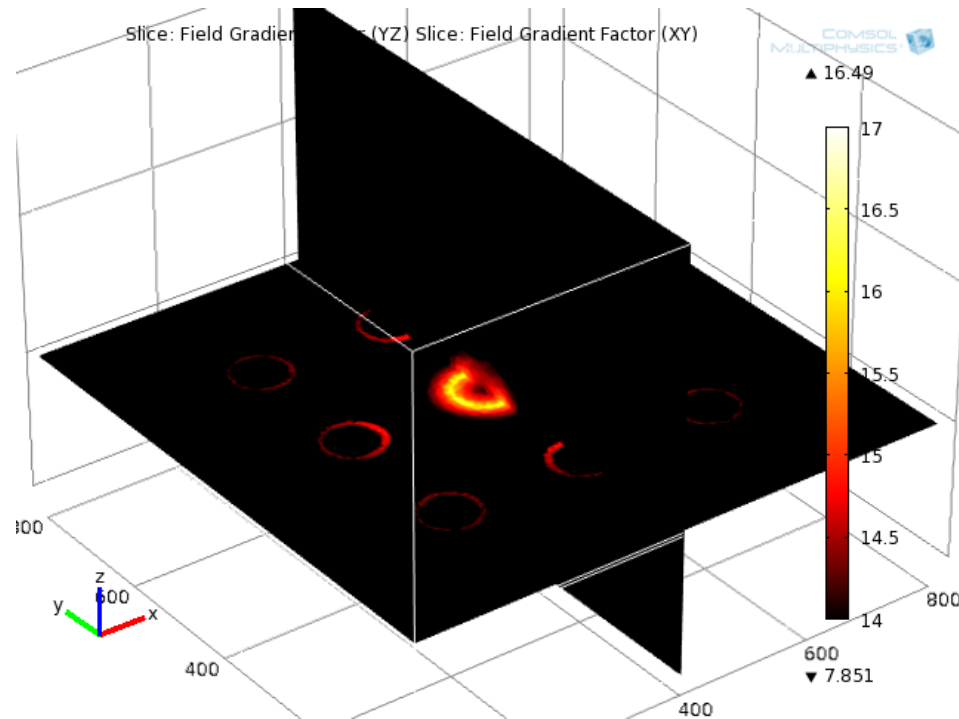

Figure 21: Field Gradient Factor of Box Pattern for 100 nm Particles. Intensity is plotted logarithmically. Areas in black fall below the minimum Field Gradient Factor for successful movement over Brownian motion.

4.2.7   Additional Electrode Configurations

A number of electrode layouts were simulated during the extent of the project, including lines, crosses, and interdigitated configurations. The checkerboard and box electrodes represent two extremes of operation; all other configurations fell in between these two in terms of either maximizing the field gradient at a single point or providing a large and dispersed active DEP area. Additional optimization of these two geometric setups for sub-micron particle concentration would require direct alteration of the

electrodes themselves, particularly their physical size and capability to withstand higher voltages and currents. The fabrication of these different electrode arrays is not covered in the extent of this project.

4.3 Separation of Fluorescent Nanoparticles from Buffer

Serial dilutions of 40 nm diameter red fluorescent polystyrene carboxylate-modified nanoparticles (Invitrogen) in concentrations ranging from 10 pg/mL to 100 ng/mL were sonicated (to disperse particle aggregates) and prepared in 1x TBE buffer (Fisher, σ = 110 mS/m) and injected into the Nanochip 100's fluidic chamber using a pipette. Concentration of the 40 nm polystyrene nanoparticles was performed using 20 V_{PP} at 10 kHz; at this frequency, the coated nanobeads experience positive dielectrophoresis (see Figure 3) and will move towards high field regions. The same procedure was performed using both the checkerboard & box electrode patterns. As the solution did not have objects that interfered with visual detection, no wash step was required. A 1x TBE buffer solution containing no fluorescent nanobeads was also analyzed under the same conditions to represent a negative control.

4.3.1   Checkerboard Configuration

Levels of increasing nanoparticle concentration were processed on an individual microelectrode array until qualitative visibility was determined. Due to the aspect ratio of the camera, the 10x objective (100x overall zoom) provides an image that includes the activated 3x3 array and three inactivated electrodes that provide a control against nonspecific binding.
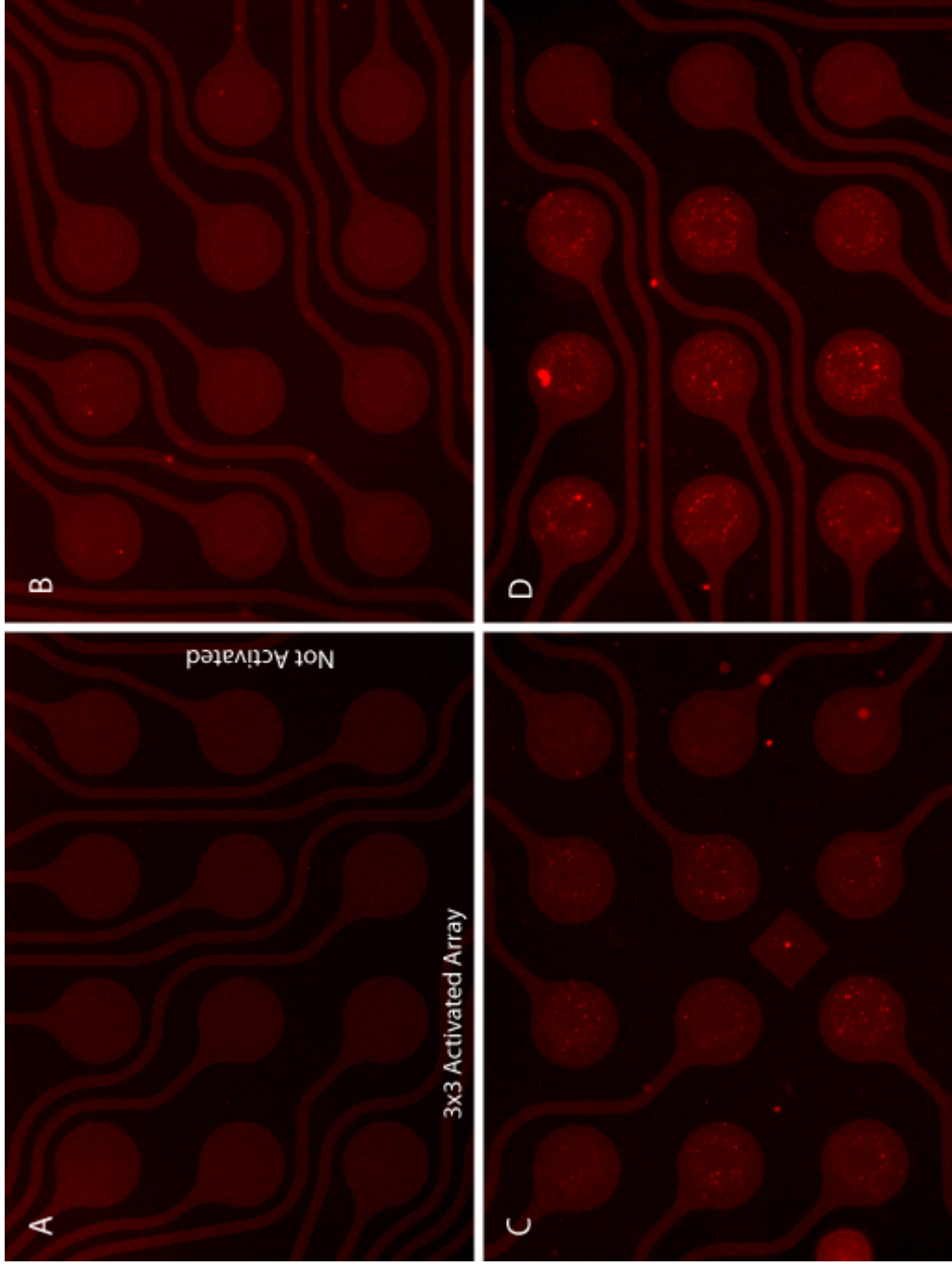
Figure 22: Concentration of 40 nm Nanoparticles from 1x TBE Buffer using Checkerboard Pattern. A) Control (no nanoparticles), B) 10 pg/mL, C) 100 pg/mL, D) 1 ng/mL. Collection performed at 10 kHz and 20 V_{PP} for 15 minutes. Images collected using a 30 second exposure at low intensity illumination. Background intensity was normalized to zero and contrast was increased 4x.

Figure 22 includes images of three dilutions of 40 nm red nanoparticles along with a control. All captured images from the CCD camera have been processed in ImageJ to aid in visualization by normalizing their black levels to zero and increasing contrast by a factor of 4. Collection of nanoparticles on the activated arrays is seen in Figure 22C, representing a particle concentration of 100 pg/mL, a level 100 times lower than the clinical goal of 10 ng/mL. The particles that have gathered are resolvable by the system, indicating that they have likely aggregated into larger clumps of nanoparticles.

Images taken before collection indicate that the majority of nanoparticles in solution have been dispersed by the sonication step prior to dilution. In the 1 ng/mL dilution, for example, there will be approximately 50,000 40 nm nanoparticles above 9 of the array electrodes (Table 2), but only a few aggregates exist prior to activation (Figure 23). Aggregation in the final images is likely due to the DEP collection process rather than other factors.
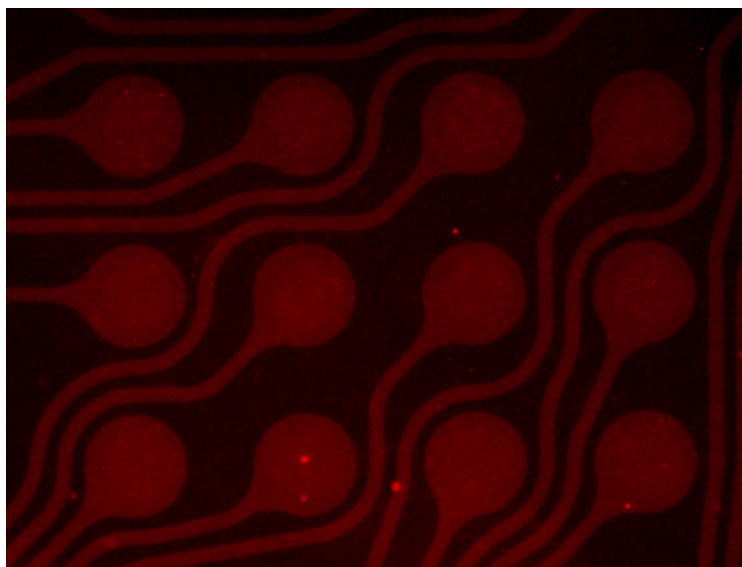
Figure 23: Image of Nanoparticle Solution before Concentration. Image taken prior to field activation using the 1 ng/mL 40 nm dilution. A few aggregated nanoparticles that survived sonication (lower center) remain in the buffer solution.

To ensure that there is a significant collection of nanoparticulates through DEP at this low level, numerical analysis of the activated electrodes against the controls is imperative. Since each individual image is taken under different conditions, including variable locations on the microelectrode array, they are not directly comparable to one another. If the electric field does not visually alter the electrodes, the inactivated electrodes on each individual image could be used as a point of comparison to the activated ones. Figure 24 shows a legend key for statistical analysis that is held constant across all captured images. Activated electrodes are indexed from A1 to A9 starting with the upper left, then moving down and to the next column to the right. Inactivated electrodes are labeled with N1, N2, & N3, starting with the uppermost electrode.
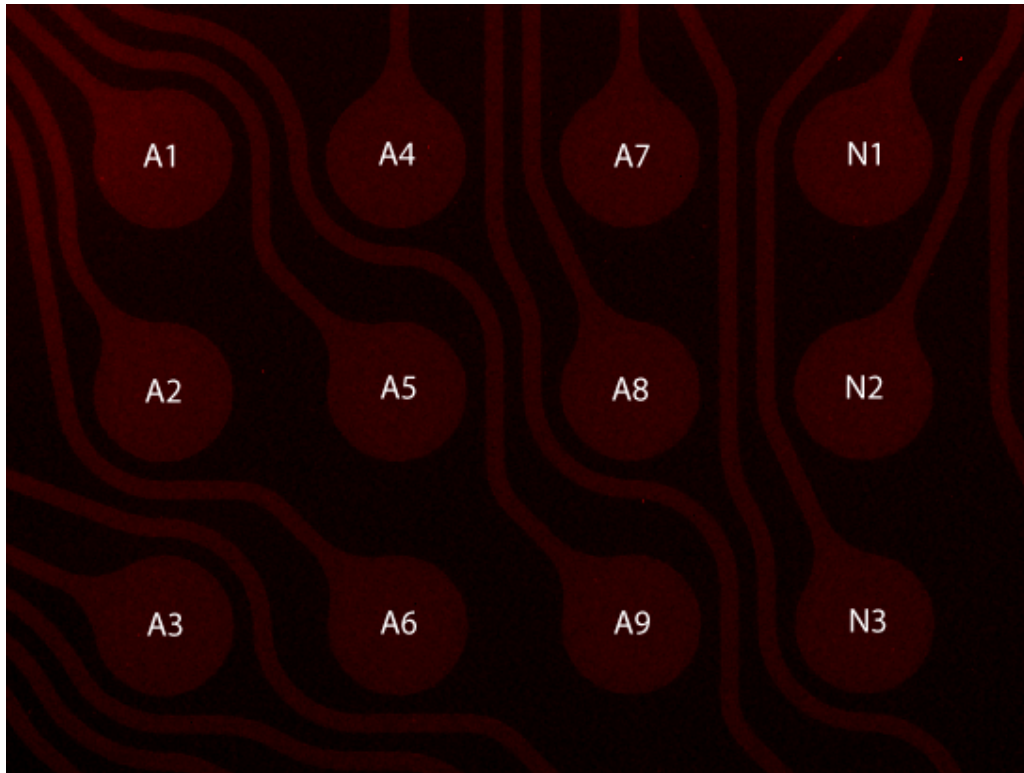
Figure 24: Legend Key for Analyzed Images. Activated electrodes are labeled A1-A9; inactivated electrodes labeled N1-N3.

Table 3: Numerical Analysis of Control Electrodes. Data was collected by outlining the individual electrode regions in ImageJ and using the histogram command (Figure 22A). The outnumbered set of four electrodes is highlighted in green.

Electrode	Control Mean	StDev
A1	14827.00	1647.00
A2	12125.78	1228.75
A3	10149.52	1184.98
A4	12170.43	1226.21
A5	10908.82	1113.72
A6	9915.23	1068.77
A7	12324.00	1172.64
A8	11065.52	1095.50
A9	10011.48	1070.67
N1	12962.37	1213.53
N2	11417.87	1168.83
N3	10002.06	1094.65
T-Test	P-Value	
A vs N	0.9710	0.5564
4A vs N	0.8960	0.9418

The mean and standard deviation was collected within each individual electrode on the control image and analyzed using a 2-tailed T-Test (Table 3). A P-Value of 0.05 represents a 95% confidence interval that the two groups are different from one another for reasons other than random distribution. For the control electrode experiment, there is no significant difference between the means and standard deviations of activated control electrodes (A) and the inactivated control electrodes (N). The outnumbered group of 4 (4A), which receive a stronger electric field and greater current density are also no different from the inactivated group. The medium does not have a visible effect on the activated electrodes; as a result, the inactivated electrodes on every individual image can be used as a control to the activated electrodes.

Table 4: Numerical Analysis of Checkerboard Electrodes with 40 nm Nanoparticles. Data was collected using ImageJ (Figure 22B-D) The outnumbered set of four electrodes is highlighted in green. T-Tests showing a 95% or greater confidence interval are highlighted in red.

Electrode	10 pg/mL Checker		100 pg/mL Checker		1 ng/mL Checker	
	Mean	StDev	Mean	StDev	Mean	StDev
A1	17173.62	1881.84	11999.33	1673.16	17582.45	4521.32
A2	15719.77	1659.10	12720.81	2507.68	19624.99	4095.99
A3	13565.36	1646.66	12835.13	2199.59	19505.91	3177.15
A4	17129.15	2062.30	12157.29	2386.77	18655.83	7980.28
A5	16896.01	1451.34	12240.96	1872.43	19476.69	3951.74
A6	15967.79	1487.79	14109.02	3388.30	20948.53	5272.02
A7	17154.95	1536.99	11758.51	1922.41	18827.12	3546.69
A8	16704.39	1507.82	12271.00	2807.29	18781.88	4074.18
A9	16219.51	1479.69	12206.76	2125.59	19096.42	3102.57
N1	16708.82	1501.77	10962.38	1456.46	14372.12	1620.19
N2	16217.24	1636.15	11237.66	1400.14	14668.18	1906.98
N3	15947.17	1529.23	11991.99	2710.79	16406.73	1852.74
T-Test	P-Value					
A vs N	0.9827	0.3513	0.0421	0.3963	0.0108	0.0007
4A vs N	0.8304	0.4316	0.0491	0.1511	0.0049	0.0297

A significant difference is found in the means for the 100 pg/mL and 1 ng/mL dilutions, and the standard deviation for the 1 ng/mL dilution (Table 4). This corresponds to the visual pattern of collection seen on the activated electrodes in Figure 22. The difference in the standard deviation (variance) for the 1 ng/mL nanoparticle dilution turns out to be as strong of an indicator of statistic significance as the comparison of the means. Since the intensity varies across each individual image due to the different utilized sections of the chip, analyzing a derivative of each collected image to focus on abrupt changes over the background may also prove beneficial.
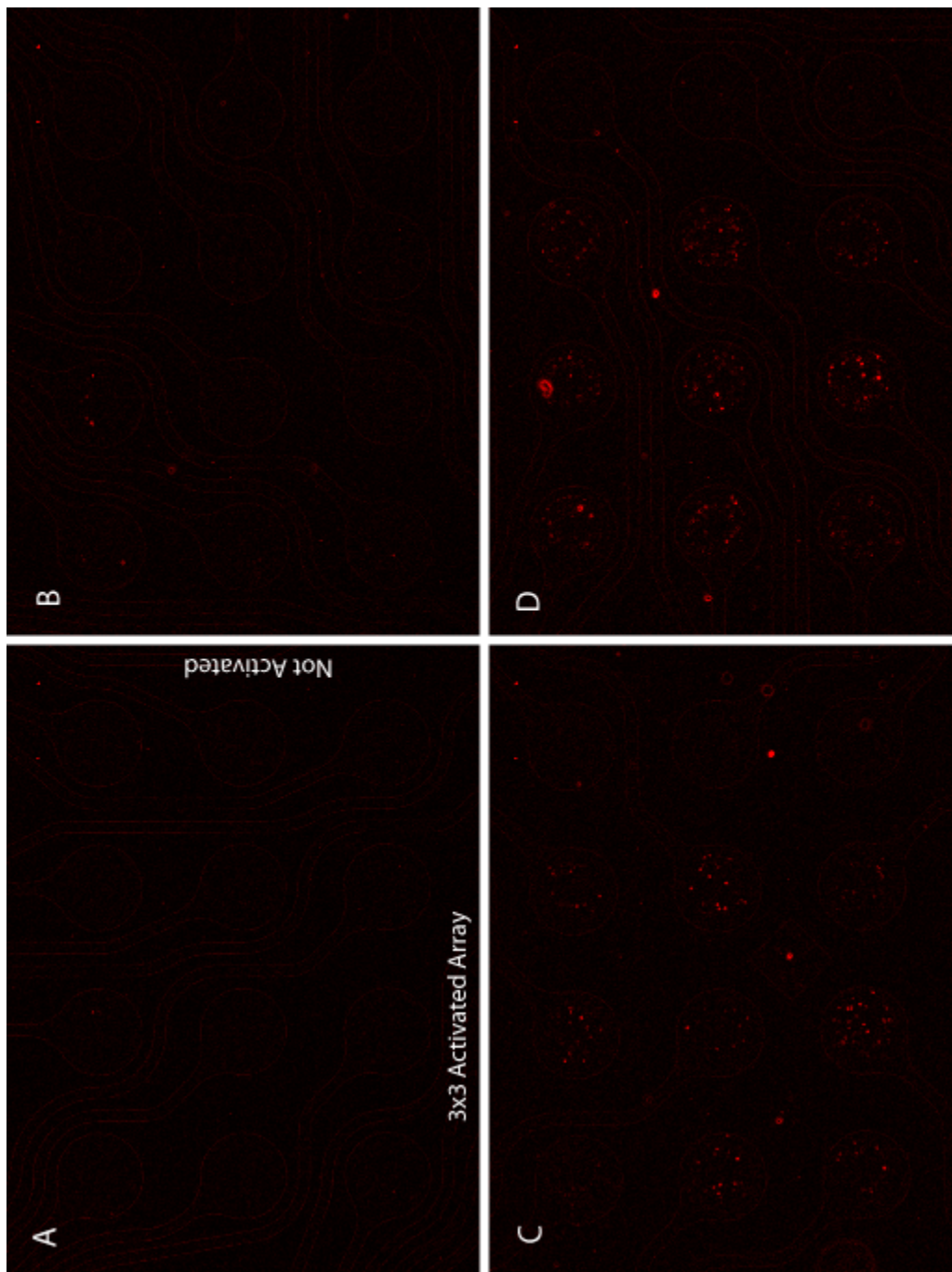
Figure 25: Derivative Images of 40 nm Nanoparticles on Checkerboard Pattern. A) Control, B) 10 pg/mL, C) 100 pg/mL, D) 1 ng/mL. The derivative image was developed by the Find Edges function in ImageJ. Background intensity was normalized to zero prior to processing and contrast doubled afterwards.

Derivative images were prepared in ImageJ from the normalized fluorescence images through the use of an edge detection algorithm; contrast was then doubled. Figure 25 shows the same conclusion as the original images: visible concentration of the nanoparticles at the 100 pg/mL and 1 ng/mL dilutions. Statistical analysis of the mean electrode intensities of these images has also been performed (Table 5); since the derivative is representative of the original variance, an analysis of the standard deviation does not provide any additional information.

Table 5: Numerical Analysis of Derivative Images of Checkerboard Electrodes. Data was collected using ImageJ (Figure 25). The outnumbered set of four electrodes is highlighted in green. T-Tests showing a 95% or greater confidence interval are highlighted in red.

Electrode	Control Checker Mean	10 pg/mL Checker Mean	100 pg/mL Checker Mean	1 ng/mL Checker Mean
A1	2489.50	2641.83	2614.40	4023.92
A2	2357.54	2463.23	3040.33	4011.28
A3	2392.74	2541.77	2893.46	3613.88
A4	2416.55	2615.52	3020.41	4683.32
A5	2327.51	2456.52	2704.69	4126.46
A6	2241.95	2437.31	3592.37	5007.71
A7	2378.77	2473.46	2804.77	3688.35
A8	2326.29	2489.96	3230.37	4275.80
A9	2227.09	2417.41	2816.55	3510.96
N1	2431.80	2457.54	2495.78	2646.78
N2	2370.97	2487.41	2379.68	2679.99
N3	2281.16	2464.14	2505.65	2712.42
T-Test	P-Value			
A vs N	0.85055	0.24594	0.00086	0.00002

Numerical analysis of the electrodes using the derivative image provides the same result as the original images: a significant difference between the activated and control electrodes are found at the 100 pg/mL and 1 ng/mL levels. Analysis of derivative

images may be valuable in place of the original captured images if intensity varies greatly across a series of images.

Compared to the original microscope system, which had a bulk detection limit at a fluid concentration of 100 ng/mL (Figures 6 & 7), the detection limit reached using the checkerboard array is three orders of magnitude lower. More impressively, the 100 pg/mL limit is 100 times lower than the clinical detection goal of 10 ng/mL.

4.3.2   Box Configuration

The dielectrophoretic concentration of the 40 nm red fuorescent nanoparticles was repeated while using the box electrode configuration (Figure 26). Unlike the checkerboard array, collection through positive DEP only occurs at the center electrode of the 3x3 array. Similar to the previous experiments, qualitative detection of nanoparticles occurs at the 100 pg/mL and 1 ng/mL dilution levels. Numerical analysis of this array configuration is more difficult due to the single electrode point at the center (A5) as a t-test requires more than one data point in order to calculate a p-value.
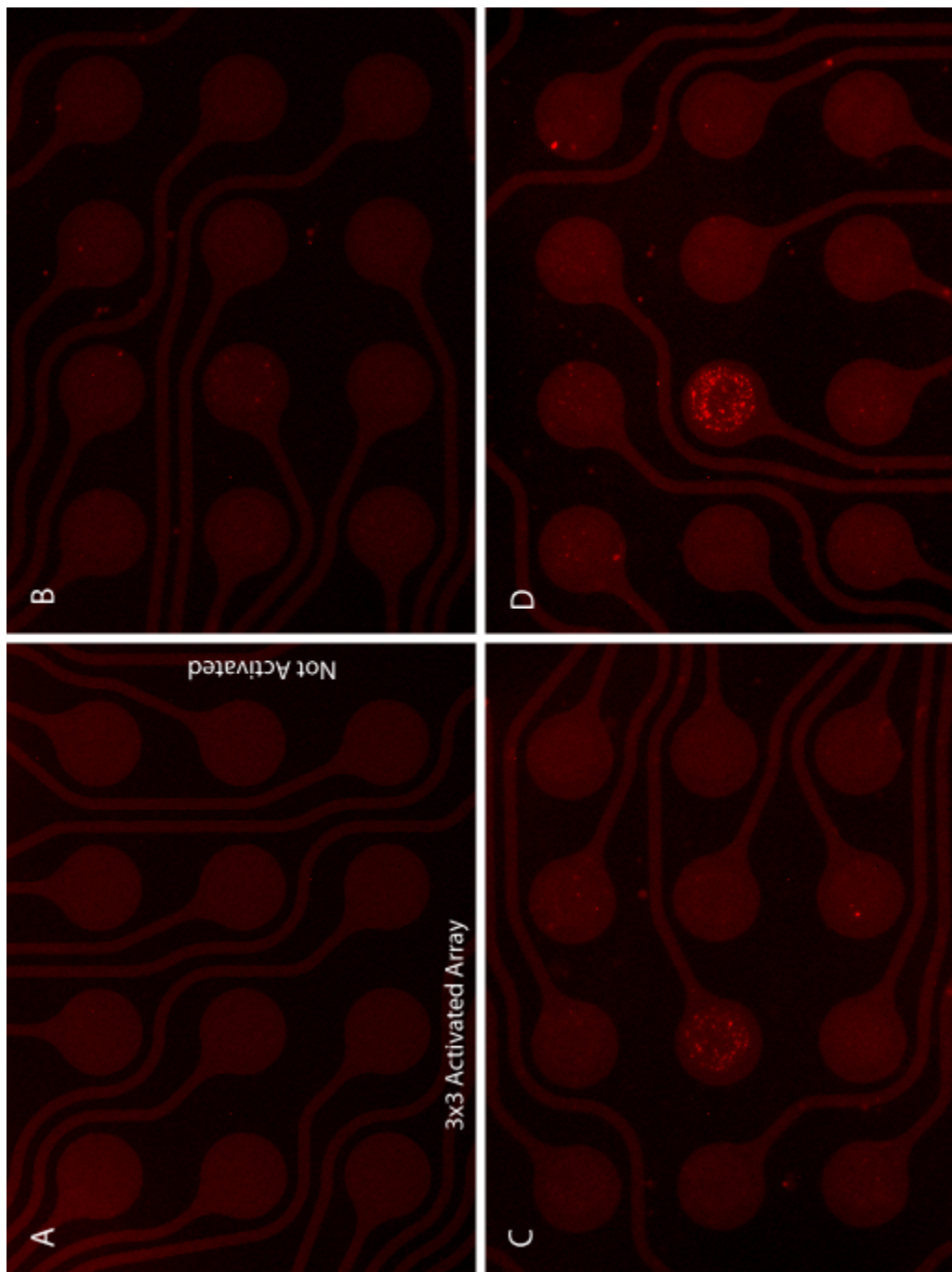
Figure 26: Concentration of 40 nm Nanoparticles from 1x TBE Buffer using Box Pattern. A) Control, B) 10 pg/mL, C) 100 pg/mL, D) 1 ng/mL. Collection performed at 10 kHz and 20 V_{PP} for 15 minutes. Images collected using a 30 second exposure at low intensity illumination. Background intensity was normalized to zero and contrast increased 4x.

The outline of the electrode edge can be easily seen through attracted nanoparticles (Figure 27). Additional particles that have been pulled onto the hydrogel over the center of the electrode can also be seen. At the 1 ng/mL dilution, a 9 electrode area will have approximately 50,000 40 nm particles in the fluid chamber above. Figure 27, on the contrary, only shows on the order of 500 resolvable spots, although most are likely to include multiple particles due to the large resolution limit (800 nm). This indicates that the collection efficiency of the system is very low, likely below 1%.
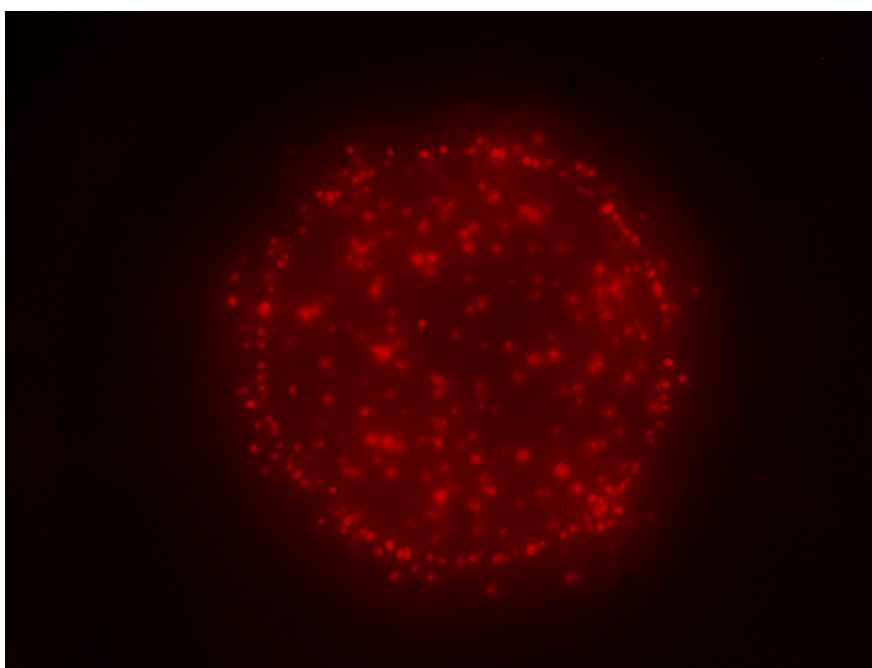
Figure 27: Fluorescence Image of Center Electrode. Taken at 500x total magnification for the 1 ng/mL 40 nm nanoparticle dilution.

Analysis of a single point can be done through a simple standard deviation test. If a data value falls two standard deviations away from the mean in a random Gaussian distribution, it can be assumed to be an outlier sitting at a 95% confidence interval. Using the three control electrodes (N) as a point of comparison for the single collection point (A5) does not create an accurate Gaussian distribution; since the 8 electrodes

surrounding the center have significantly reduced collection efficiency, they can be used

in their place.

Table 6: Numerical Analysis of Box Electrodes with 40 nm Nanoparticles. Data was collected using ImageJ (Figure 26). The center electrode is highlighted in green. If the intensity of the center electrode exceeds the 95% confidence interval (over two standard deviations from the mean), the confidence interval is highlighted in red.

Electrode	10 pg/mL Box Mean	StDev	100 pg/mL Box Mean	StDev	1 ng/mL Box Mean	StDev
A1	10482.30	1326.62	10133.94	1357.92	13899.61	2396.64
A2	10040.04	1445.55	10093.19	1370.69	12785.31	1520.54
A3	9461.07	1388.64	10672.23	1569.47	13150.22	1740.26
A4	10142.37	1617.11	11194.56	1503.68	14269.57	1937.75
A5	10319.84	1752.05	14028.00	4356.51	21390.78	8904.52
A6	9489.79	1297.00	12979.47	1570.28	14559.96	1948.51
A7	10089.23	1563.85	12810.56	1738.79	15182.63	1994.44
A8	9892.66	1341.83	12523.18	1376.35	15583.80	1885.90
A9	9726.93	1297.12	13121.96	2420.47	14441.21	1596.34
Statistics						
Mean A	9960.47	1447.75	11950.79	1918.24	15029.23	2658.32
Std.Dev A	351.34	161.85	1447.83	971.57	2544.24	2356.09
95% Conf. A	10663.15	1771.45	14846.45	3861.38	20117.72	7370.49

At the 1 ng/mL dilution level, the mean and standard deviation values of the

center electrodes fall outside of the 95% confidence interval. Although significant

collection is visible in the 100 pg/mL image, only the standard deviation of the A5

electrode is outside the confidence interval. In line with the analysis of the checkerboard

images, a set of derivative images were also calculated and analyzed (Figure 28 & Table

7). Analysis of the derivative images indicates the same result as the originals:

significant concentration of nanoparticles has occurred at the 100 pg/mL and 1 ng/mL

levels.
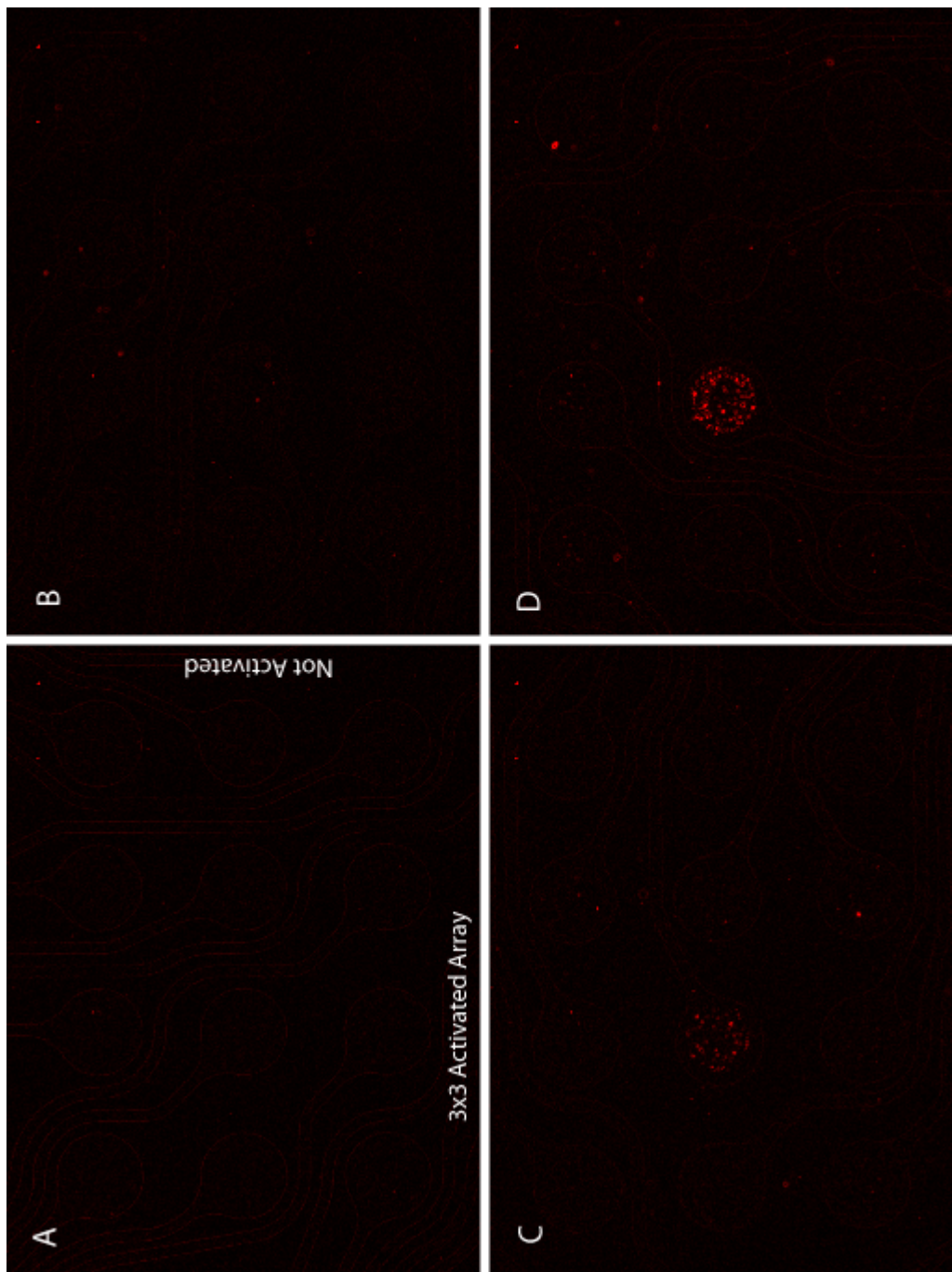
Figure 28: Derivative Images of 40 nm Nanoparticles on Box Pattern. A) Control, B) 10 pg/mL, C) 100 pg/mL, D) 1 ng/mL. The derivative image was developed by the Find Edges function in ImageJ Background intensity was normalized to zero prior to processing and contrast doubled afterwards.

Table 7: Numerical Analysis of Derivative Images of Box Electrodes with 40 nm Nanoparticles. Data was collected using ImageJ (Figure 28). The center electrode is highlighted in blue. If the intensity of the center electrode exceeds the 95% confidence interval (over two standard deviations from the mean), the confidence limit is highlighted in red.

Electrode	10 pg/mL Box Mean	100 pg/mL Box Mean	1 ng/mL Box Mean
A1	2442.78	2489.03	2885.21
A2	2462.12	2388.10	2618.42
A3	2486.80	2495.80	2624.30
A4	2549.79	2512.56	2715.36
A5	2543.42	4320.59	8637.72
A6	2387.94	2467.52	2771.27
A7	2503.79	2558.88	2760.10
A8	2409.07	2465.07	2676.70
A9	2392.21	2660.97	2548.45
N1	2426.55	2409.50	2974.70
N2	2374.91	2354.79	2557.32
N3	2420.89	2388.76	2583.37
T-Test			
Mean A	2464.21	2706.50	3359.73
Std.Dev A	61.42	609.84	1981.75
95% Conf. A	2587.05	3926.18	7323.22

The box electrode configuration, at the onset, was hypothesized to be a better choice for concentration of low levels of particulates. After analysis of the checkerboard and box patterns, the detection capability was found to be the approximately the same (100 pg/mL). The intensity of the box's center electrode in the derivative image is approximately four times higher than the surrounding electrodes, while the checkerboard equivalent is only 20% higher. Since the center point is more easily distinguishable, it is likely that the box electrode pattern has a slightly lower detection limit than the checkerboard, but this has not been investigated further.

The physical simulations performed for the checkerboard (Figure 16) and box (Figure 21) electrode geometries help to explain why the detection limits are similar. The box configuration has a larger collection point at the center, but suffers from a lack of total active volume; only a single electrode has a strong enough force to induce trapping. The checkerboard pattern provides a far larger active interrogation volume and is more likely to concentrate a higher number of nanoparticulates into the high field regions.

The checkerboard array is better suited for robust statistical tests due to a higher number of comparable electrodes. Since the checkerboard provides a greater separation potential, it is a better overall choice for subsequent tests using any type of mixed media. Although the result for the box pattern is not improved over the checkerboard, the improvement in the low level detection limit remains: three orders of magnitude over the bulk fluorescence.

4.4 Separation of Nanoparticulates from Blood

Experiments using fluorescent nanoparticles in buffer have proven that a combined microscope & DEP powered array can reach detection limits lower than the 10 ng/mL level for normal DNA in human blood. Although this is a noteworthy statement in favor of the complete analytical system, the performance of the system with a complex medium is unknown.

Blood is one of the most complex biological samples available, containing multiple cell types, cellular debris, and a high level of protein. It serves as an important diagnostic tool for infectious and degenerative diseases, bodily injury, and other disorders[11]. As a varied medium, it provides a great challenge to the DEP powered microelectrode array. The high ionic content in blood causes it to have a conductivity of

approximately 0.5 S/m[12], almost 5 times higher than 1x TBE buffer (110 mS/m). As stated in Section 2.2, DEP is considerably weaker in high conductance media due to a reduced Clausius-Mossotti factor for suspended particles. The complex nature and high conductance of blood create a difficult test for the system.

4.4.1 Nanoparticles from Whole Blood

Samples of blood from healthy individuals were provided by the Kipps Lab at the Moore's Cancer Center (University of California, San Diego) and spiked with carboxylate-modified red and green fluorescent polystyrene nanoparticles (Invitrogen). Serial nanoparticle dilutions were prepared in 1x TBE buffer (Fisher) and mixed with a sample of whole blood at a 1:9 ratio. Concentration levels of 10 pg/mL, 100 pg/mL, 1 ng/mL, and 10 ng/mL were tested along with a negative control. Nanoparticle diameters of 20 nm, 40 nm, and 100 nm were all used independently over the course of multiple experiments. The DEP frequency was held constant to previous experiments (10 kHz), but the applied voltage was reduced to 14 V_{PP} to compensate for the higher medium conductivity (~1 S/m) and possible bubbling due to joule heating. The high concentration of cells in blood makes the sample opaque, so a series of three buffer washes were performed after the separation to remove all undesired cellular material. The DEP field was left activated during the wash steps to maintain trapping of nanoparticles on the microelectrode array.

Although the conditions were configured to induce positive DEP on the nanoparticles spiked into the blood, all of the tests performed with whole blood were inconclusive and did not provide reliable results. Concentration levels equal to and significantly higher than the beads-from-buffer limit of 100 pg/mL did not show adequate qualitative collection. Collection of nanoparticles from high conductance buffers has

been demonstrated through prior work[3], but was not established in these series of tests. Other possible explanations for the lack of collection include interference from components of the blood sample, and the removal of collected nanoparticles with the required wash steps.

4.4.2 Nanoparticles from Blood Cells

At a frequency of 10 kHz, cellular material is expected to be influenced by negative DEP, driving it away from the active electrodes, while the coated nanoparticles are expected to continue to be concentrated under positive DEP (Figure 3). To ensure that this process was still occurring, a blood sample was placed in a centrifuge at 8000 RPM for 3 minutes to separate the blood cells and the plasma. 20 uL of red blood cells were extracted from the spun sample and mixed with 880 uL of 1x TBE and 250mM Sucrose buffer (to prevent cell lysis) and 100 uL of 20 nm green fluorescent nanoparticles at a 100 ng/mL dilution. The separation of the blood cells and 20 nm nanoparticles (10 ng/mL final concentration) was performed at 10 kHz and 20 V_{PP} for 20 minutes.

A bright field image taken at the end of the 20 minute collection period (Figure 29A) shows strong negative DEP of all cells in the solution mixture, indicating that cellular material is pushed away from the high field regions. A fluorescence image taken after three wash steps (Figure 29B) contains three faint rings surrounding the A2, A4, and A8 electrodes, qualitatively indicating the concentration of green nanoparticles. The blood cells have not prevented separation from occurring, and the wash steps have not removed all of the nanobeads from the surface of the hydrogel. Figure 30 shows a 50x magnification image of the A8 electrode; nanoparticles can be faintly seen collected around the edge of the active electrode.
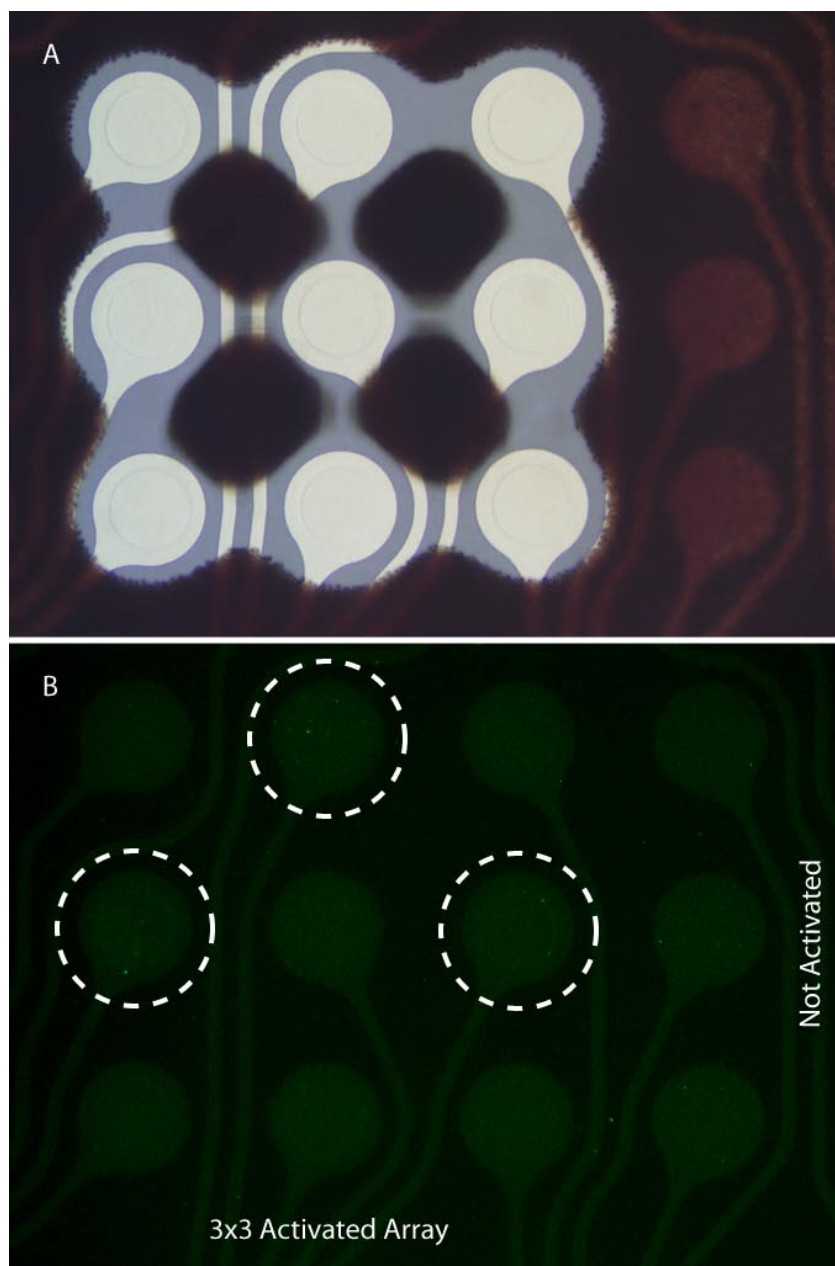
Figure 29: Separation of 20 nm Green Nanoparticles from Red Blood Cells. A) Bright field image taken after 20 minute separation, B) Fluorescence image taken after two fluidic washes. Sample contained 2% RBC suspended in 1xTBE w/ 250 mM Sucrose and 10 ng/mL of 20 nm green nanoparticles. Separation performed with 20 V_{PP} at 10 kHz for 20 minutes.

Numerical analysis of the green fluorescence image (Figure 29B) did not provide

any statistical significance, so no quantitative conclusion can be made. In the previous

experiments involving the detection of nanoparticles in buffer, a concentration level of 1 ng/mL can be clearly seen on both the checkerboard and box electrode patterns. In comparison, a 10 ng/mL concentration of 20 nm green nanoparticles in a 2% solution of red blood cells provides a significantly weaker result. Since the wash is not removing all of the nanoparticles from the hydrogel and collection in high conductance buffers has been previously demonstrated, interference within the medium (blood) itself becomes a likely cause.
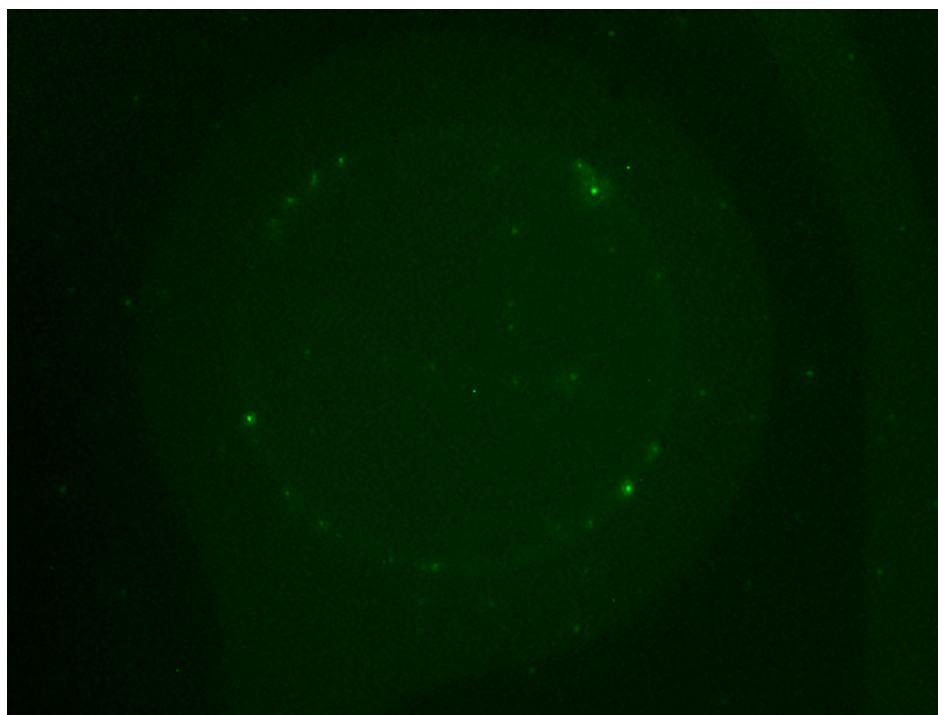
Figure 30: Image of Single Electrode with Collected 20 nm Green Nanoparticles. Image taken at 500x magnification (50x objective) with a 30s exposure time.

The nanoparticles used in the buffer and blood experiments are coated with exposed carboxylate groups, which increase the surface charge of the particle and provide a net negative charge. This is of benefit for modeling purposes, as the size and negative charge of the nanoparticles is a strong corollary to important biological

molecules such as DNA. An undesirable consequence of the carboxylate coating is the possibility of either specific or nonspecific binding. For example, if a carboxylate group comes into contact with an amine group under the presence of an enzyme, it may create a polar covalent peptide bond and form a larger macromolecule[13].

Any amino acid or protein with an exposed amine group, or another net positively charged molecule, is a possible binding site for a carboxylate group. Blood contains a high concentration of free protein in addition to surface proteins found on the surface of white and red blood cells. The total concentration of protein in blood plasma is extremely high, ranging from 60 to 80 mg/mL; this number dwarfs the tested nanoparticle dilutions by 7+ orders of magnitude[14]. If the carboxylate coated nanoparticles are being bound to cells or blood proteins and carried away from high field regions, it would explain the lack of results when attempting to concentrate them from a normal blood sample. A neutral alternative that does not bind directly to proteins in blood is required in place of the selected nanoparticles.

4.4.3 DNA from Whole Blood

Unlike the carboxylate-modified polystyrene nanobeads, DNA is normally found in the human blood as a result of illness, injury, or cellular death. Although human DNA is generally found with structurally supporting proteins (histones), it can be purified from blood samples through a number of procedures. The DNA molecules themselves will not freely bind to proteins, making them less likely to be carried away alongside particulates under negative DEP. The separation of high molecular weight DNA (>1,000 base pairs) from low and high conductance buffers has also been previously demonstrated[3].

A normal blood sample of 900 ul was mixed with 100 uL mixtures of DNA (in 1x TBE buffer) labeled with SYBR green dye (4x concentration) and run on the microelectrode array using the same conditions as the previous whole blood experiments. Three wash steps were performed following the sample removal with the electric field held active. Two dilutions of 48 kilobase lambda phage DNA at 20 pg/mL and 200 pg/mL, and one dilution of 400 base pair DNA fragments at 200 pg/mL were run alongside a negative control. Neither of the DNA samples contained any structural or supporting proteins.

DNA is typically described in terms of base pair length rather than physical dimensions due to polymer chain behavior. Short chains behave as rigid rod-like structures, while longer chains are flexible and may fold upon themselves to form a dense structure. The transition point between these two phases is defined as the persistence length. The lambda phage and 400 base pair DNA fragments spiked into the blood samples are double-stranded DNA (dsDNA), which has a persistence length of 50 nm[15]. One unit cell of a dsDNA coil is composed of 76 base pairs, extending a distance of 21.86 nm; utilizing this value, the persistence length can be approximated to a length of 180 bp. As the fragments utilized fall above this length, they can be assumed to act as a flexible chain rather than a rigid cylindrical structure.

If placed in an applicable solvent (water), each base pair of the dsDNA occupies a volume of 2,047 $Å^3$ (2.047 nm^3)[16]. When the 400 bp and 48 kb fragments are compressed to this minimum limit, they will occupy volumes of 818.8 and 98,256 nm^3, respectively. If the DNA chains assume a spherical shape, the 400 bp sphere will have a diameter of approximately 11.6 nm, while the 48 kb lambda phage DNA will have a

diameter of approximately 57.25 nm. The diameters in solution are likely to be larger due to additional solvent hydration and random walk of the polymer chain.

The microelectrode array has been demonstrated to have the capability to concentrate polystyrene nanoparticles at and above 20 nm in diameter, but not below. If the 400 bp DNA fragments are close to their minimum packing diameter of 11.6 nm they may be too small to overcome Brownian motion and be effectively concentrated by DEP. The lambda phage DNA, on the contrary, occupies a 60 nm or larger diameter sphere, which falls above the 20 nm size limit.

Images captured after separation for all four tests are shown in Figure 31. Unlike the nanoparticle experiments, the dye cannot be easily seen at low intensity exposures and is partially overwhelmed by background noise. To resolve this problem, the images have been captured using high intensity illumination and a 1 second exposure time.
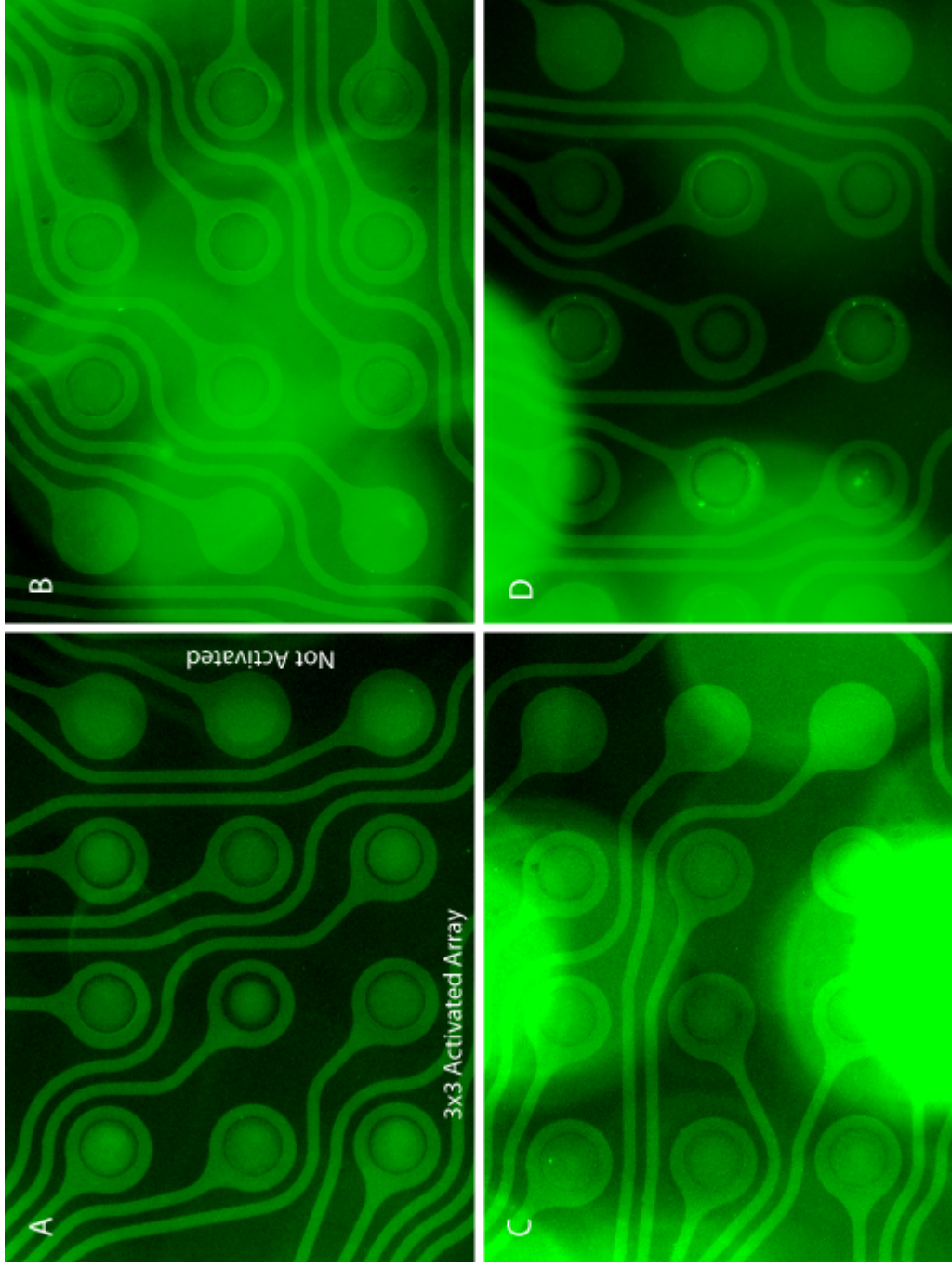
Figure 31: Separation of DNA from Whole Blood. A) Control; B) 200 pg/mL of 400 bp DNA (inactivated electrodes are in the left column); C) 20 pg/mL of 48 kb lambda DNA; D) 200 pg/mL of 48 kb lambda DNA. Images were collected using a 1s exposure at high intensity, have had their black level normalized, and contrast increased by a factor of 4. Collection performed at 14 VPP & 10 kHz for 14 minutes.

Possible collection can be seen at the 200 pg/mL level for the lambda phage

DNA, but the collected images are covered in interfering intensity. Cellular debris in the

blood has bonded with free dye molecules and stuck to the surface of the top of the

fluidic channel, causing a large amount of each image to be covered in a series of bright

spots. This out of focus interference is a major limitation of wide field microscopy, but

must be dealt with. Previous analysis of captured images has shown that derivative

(edge detection) images can compensate for differences in bulk intensity. By looking at

abrupt changes in intensity, the collection may be more easily detected and analyzed.
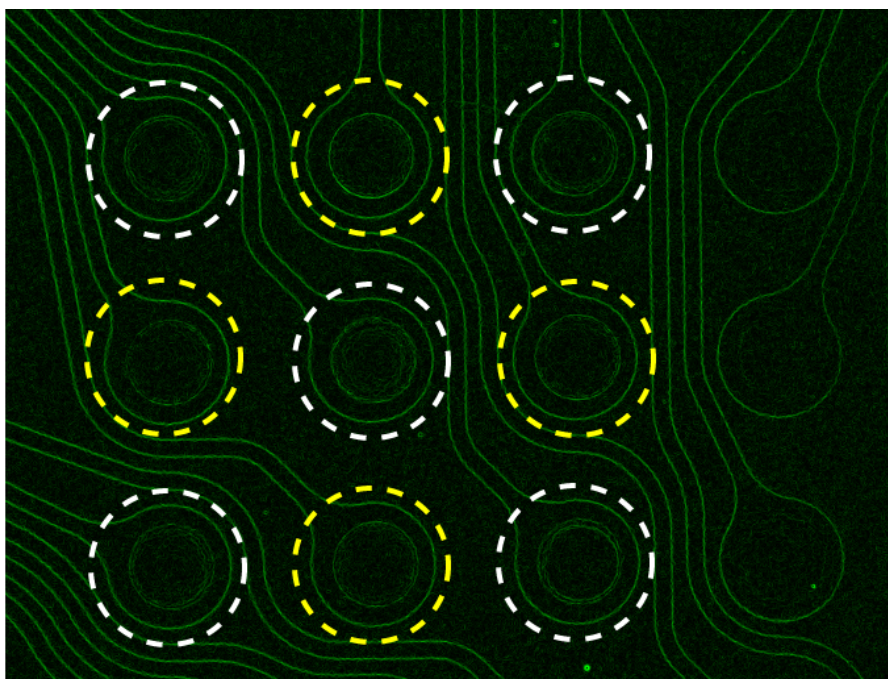
Figure 21: Derivative Image of Whole Blood Control. Outnumbered set of 4 electrodes outlined in yellow.

Figure 32 shows a derivative image of the negative control sample, which

contains 90% whole blood, a 10% mixture of 1x TBE, and a 4x concentration of SYBR

Green fluorescent dye. A faint intensity spot seen on the original image (Figure 31A)

around electrode A7 has been removed through processing, resulting in a smoother

appearance. Statistical analysis of the control image to compare the activated and

inactivated electrodes through a t-test has been performed (Table 8).

Table 8: Numerical Analysis of Derivative Control Electrodes using Whole Blood. The outnumbered set of four electrodes is highlighted in green. Data collected using ImageJ from Figure 32. Significant T-Test results (95% confidence) are highlighted in red.

	Control
Electrode	Mean
A1	3178.41
A2	3035.14
A3	3158.82
A4	3440.62
A5	3423.07
A6	3087.28
A7	3349.13
A8	3102.15
A9	3246.21
N1	2518.90
N2	2587.87
N3	2582.20
T-Tests	P-Value
A vs N	2.80E-07
4A vs N	5.73E-03

Unlike the previous experiments pulling nanoparticles out of buffer, the

application of an electric field in blood causes a significant appearance change in the

activated electrodes that shows up during numerical analysis. As a result, the inactivated

electrodes cannot be used as a direct comparison to active electrodes on any individual

image.
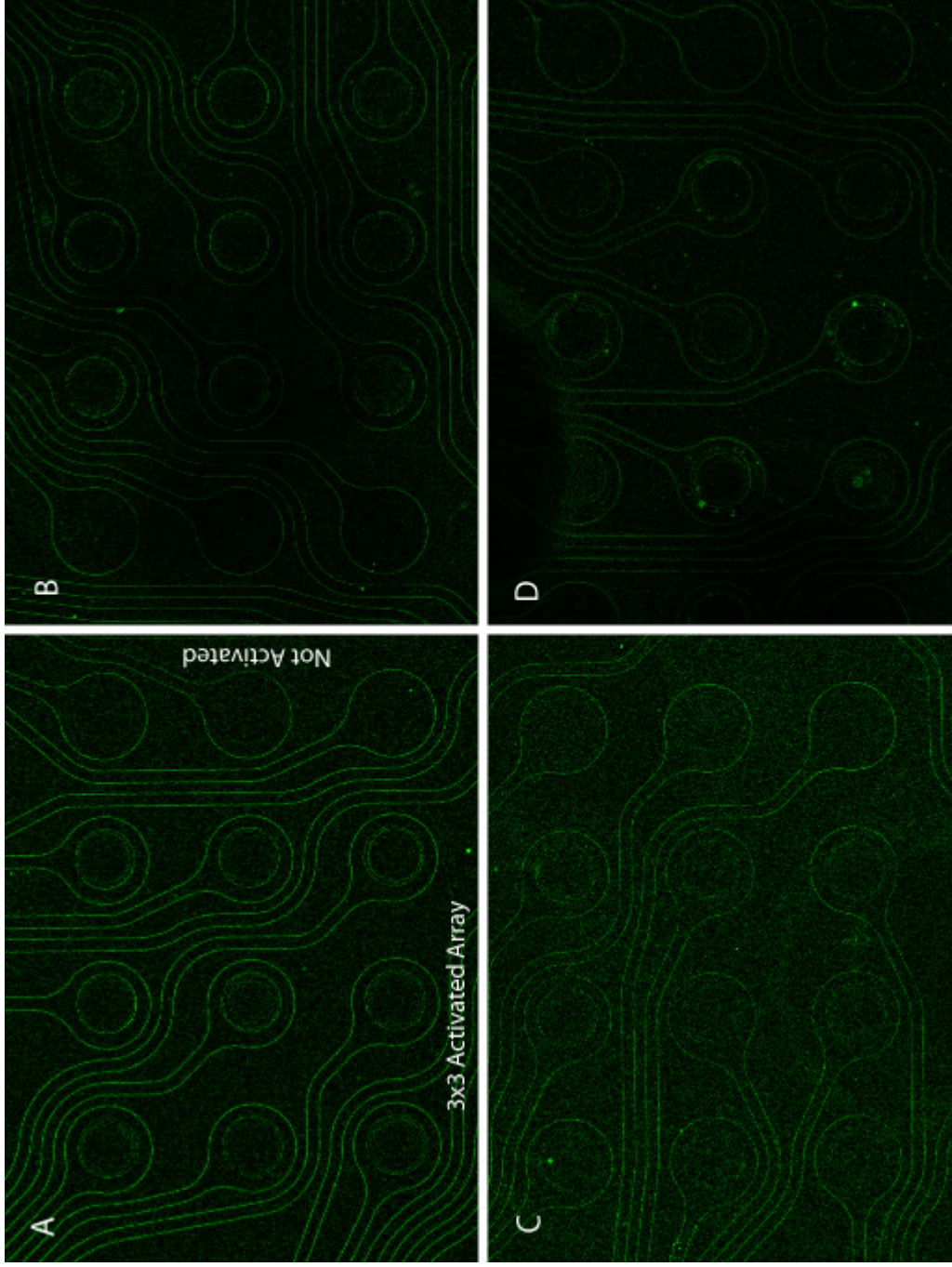
Figure 33: Derivative Images of Separation of DNA from Whole Blood. A) Control; B) 200 pg/mL of 400 bp DNA (inactivated electrodes are in the left column); C) 20 pg/mL of 48 kb lambda DNA; D) 200 pg/mL of 8 kb lambda DNA. Derivative image generated through the Find Edges command in ImageJ. All images had their black level normalized prior to processing, and their contrast doubled afterwards.

Processing the image through derivation has removed the high intensity noise in the original images, providing clearer visualization. No variance surrounding the activated electrodes is seen on the 200 pg/mL 400 bp (Figure 33B) or the 20 pg/mL lambda phage (Figure 33C) derivative images. Spikes of intensity are seen surrounding the outnumbered set of 4 electrodes in the 200 pg/mL lambda phage DNA image (Figure 33D), corresponding to a slight halo seen surrounding them in the original image (Figure 31D). Concentration of the spiked DNA is likely, but the activated electrodes cannot be numerically compared to the inactivated control electrodes in the right column. Upon further investigation, the potential collection is almost completely concentrated surrounding the four outnumbered electrodes in the checkerboard pattern. The controls cannot be used as a point of comparison, but the opposing sets of active electrodes can.

Table 9 Numerical Analysis of Derivative Electrodes with Whole Blood. Data collected from Figure 33. The outnumbered set of four electrodes is highlighted in green. Significant T-Test results (95% confidence) are highlighted in red.

Electrode	Control Mean	400 bp DNA 200 pg/mL Mean	Phage DNA 20 pg/mL Mean	Phage DNA 200 pg/mL Mean
A1	3178.41	4277.03	4500.74	3373.36
A3	3158.82	3462.25	4315.71	3482.30
A5	3423.07	3406.60	4175.28	3410.97
A7	3349.13	4686.90	4506.54	2873.03
A9	3246.21	4294.16	4419.98	2792.05
A2	3035.14	2217.85	4408.21	3899.01
A4	3440.62	3135.92	4253.61	4133.80
A6	3087.28	3144.44	4299.24	4177.41
A8	3102.15	4347.69	4306.37	3530.95
N1	2518.90	3341.56	3954.19	2689.58
N2	2587.87	1875.68	4268.27	2306.15
N3	2582.20	2175.11	4015.92	2323.72
T-Test	P-Value			
5A vs 4A	0.3682	0.1684	0.3807	0.0091

There is no statistical significance found between the set of 4 (4A) and set of 5 (5A) activated electrodes for the control (no spiked DNA), 400 base fragments, and the 20 pg/mL dilution of the 48 kb lambda phage DNA. At the 200 pg/mL phage DNA dilution (Figure 33D), however, there is a significant difference between the two opposing sets of active electrodes, indicating that collection has occurred. Looking back to the simulations of the checkerboard array (Figures 9 & 13), it is expected for the outnumbered electrodes to have a stronger trapping potential due to higher electric field and current density. Thus, the results line up well with the original theory of operation.

The 400 base pair DNA fragments were not successfully concentrated out of the blood sample (Figure 33B) and captured on the microelectrode array. As previously noted, it is likely that the fragments were too small, preventing the induced DEP force from overcoming simple Brownian motion. This is significant, given that the normal level of DNA in human blood is approximately 10 ng/mL, and the detection level reached with the lambda phage DNA was successful at a 50 times lower concentration. The majority of DNA in human blood is from controlled cellular death (apoptosis) and generally broken down into small fragments shorter than 500 bp[11]. The array geometry does not support the collection of these small fragments but does allow large pieces of spiked (HMW) DNA to be concentrated directly out of a blood sample. The size cutoff prevents the lambda phage DNA from being overwhelmed by small intrinsic DNA fragments.

The lowest effective level reached with spiked DNA in blood with the checkerboard array pattern has been demonstrated to be 200 pg/mL, similar to the previous level reached with nanoparticles concentrated out of buffer solution (100 pg/mL). The addition of the microelectrode array to the epifluorescent microscope has

improved upon the bulk detection limit by three orders of magnitude. More importantly, the limits reached are 50 to 100 times lower than the clinical goal of 10 ng/mL set forth at the onset.

4.5 Summary of Experiments

Table 10: Summary of Results

Particle Concentration	Experimental Notes & Results
1 ug/mL	Logarithmic Scaling of Fluorometer Ends
100 ng/mL	**Bulk Fluorescence Limit of Microscope** Detection Limit of Fluorometer
10 ng/mL	**Clinical Detection Goal: Normal Level of DNA in Human Blood** Separation of 20 nm Nanoparticles from Red Blood Cells
1 ng/mL	Significant Concentration of: **HMW DNA from Whole Blood via Checkerboard (200 pg/mL)** 40 nm Particles from Buffer via Checkerboard (100 pg/mL) 40 nm Particles from Buffer via Box Pattern (< 100 pg/mL)
100 pg/mL	

Through the use of the analytical system (microscope and microelectrode array), statistically significant collection of nanoparticles from buffer and HMW DNA from blood has been established at mass concentrations down to 100 pg/mL. This level is a thousand-fold improvement over both the microscope's bulk capability and the performance of a specialized fluorometer. The original clinical goal of 10 ng/mL was not only met, but exceeded by two orders of magnitude. Improvements in the performance of the array would likely increase its capability even further.

Chapter 5: Future Work & Conclusions

5.1 Conclusion

A base epifluorescent microscope lacks the sensitivity to detect extremely low levels of analytes in biological and environmental samples due to a combination of limited optics and a low cost detector. Wide field images collected through the epifluorescent system have resolution and noise limitations that limit their detection performance compared to high precision systems, such as scanning confocal microscopes. The low cost and widespread penetration of epifluorecent microscopes into laboratory settings, however, makes them a strong candidate as part of an integrated analytical system designed specifically for low level detection.

In this research, an epifluorescent microscope was paired with a microelectrode array capable of different electrokinetic separation and concentration processes. The most important of these processes, dielectrophoresis, provides selective concentration and separation of dielectric particles by changing applied voltage and frequency. Instead of changing the optical system to better detect an existing sample, the sample has had it appearance modified to better suit the existing system. The combined epifluorescent microscope & microelectrode array system costs less than one fifth the amount of a scanning confocal microscope[2].

The results of this exploratory testing are very impressive. Fluorescent nanoparticles have been concentrated from buffer solution to a level of 100 pg/mL, a 1000 times lower level than the microscope's bulk detection limit. Labeled high molecular weight DNA has been separated from human blood at a level of 200 pg/mL,

500 times lower than the bulk limit. More importantly, these concentration limits are 50 to 100 times lower than a clinically relevant detection limit in medicine, the normal level of DNA in the blood of a healthy human individual (10 ng/mL)[11]. The dielectrophoresis powered microelectrode array has been shown to effectively concentrate and separate targeted particles from clean and mixed media without harming the interrogated sample.

The analytical system composed of the basic epifluorescent microscope and the dielectrophoresis-powered microelectrode array has been established to have the capability to detect nanoparticulates below levels of clinical importance. Given the low cost of the system compared to alternate methods, a streamlined commercial electrode array system for research and clinical use could be an important tool for the low level monitoring of drug delivery nanoparticles, injury, disease, and environmental contamination.

5.2 Future Work

Although the analytical system has performed admirably in reaching a detection limit one thousand times lower than the microscope's bulk capability, it is in no way a streamlined or optimized device. The 100 site microelectrode array used for this project, for example, was originally designed for low voltage DNA binding and hybridization experiments and does not have the capability to handle large voltages or currents. It has additional limitations, primarily involving the fluidics surrounding the array. The height of the chamber is over twice as high as the maximum extension of the electric field, and there is an extremely large dead fluid volume that is not interrogated.

The addition of a new fluidics system to the microelectrode array would go far in attempting to unleash its full capabilities. A smaller and more streamlined fluidic

chamber above the chip would increase the concentration capability of the chip on a per-volume basis. Adding a fluidic pump, such as a low rate syringe pump, to slowly move a larger volume through the active area of the chip, will also increase the concentration capability of the system. On the electronic side, the investigation of alternate waveforms, such as square or triangle waves, may prove valuable. Square waves of different duty cycles, the proportional difference between the positive and negative states, have been shown to benefit the selective alignment of carbon nanotubes[18]. Swapping electrode geometries during operation to provide additional specialization and capability is also a potential option.

Optimization of the array geometry is a major point of improvement. The utilized microelectrode array was made of a fixed array of circles, with all of them possessing the same size and pitch. The checkerboard electrode configuration was found to be the best option due to the large amount of volume that it interrogated even though the box pattern was a better theoretical performer for single point concentration. The box configuration exhibited a reduced total active volume that limited its capability during experimentation. Variations on the size, spacing, and geometry of the electrodes have the potential to overcome the limitations of these basic geometries.

Optical systems can be engineered for imaging or maximum power transfer; likewise, the microelectrode array can be designed to promote separation, concentration, or a middle ground between the two. The checkerboard pattern has proven to be a strong choice for separation potential due to a high active volume. A simple modification in the geometry of the electrodes themselves, such as the one presented in Figure 34, could be made in a future electrode array.
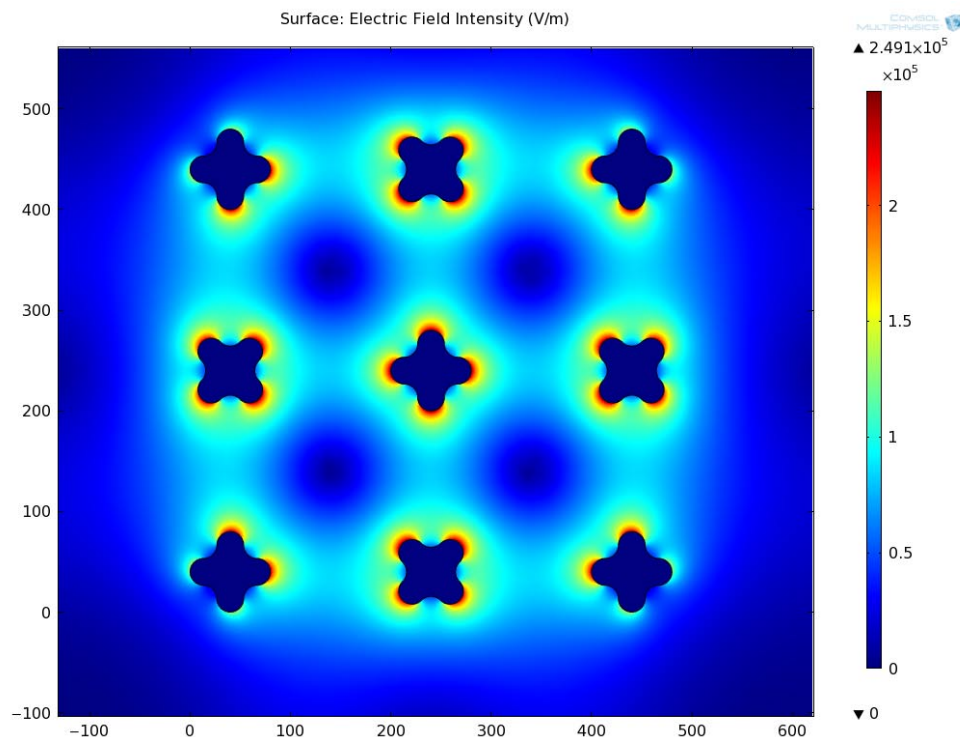
Figure 34: Electric Field Plot of Hypothetical Elliptical Electrodes. Electrode polarities configured in a checkerboard pattern

In this configuration, the 80 micron circular electrodes have been replaced with a set of 80 micron (end-to-end) interlocking elliptical electrodes that alternate their rotation by 45 degrees. In this configuration, rather than having a ring of high field collection (positive DEP) surrounding the electrode, the high field region is concentrated at four opposing points. In practice, this should provide the same maximized active volume as the circular checkerboard, but help to concentrate target analytes into sharper points instead of a general circular region. Shrinking the total dimensions of the array would also be beneficial in helping collect smaller sized nanoparticulates.

References

1. N.S. Claxton, T.J. Fellers, M.W. Davidson, in: J.G. Webster (Ed.), Encyclopedia of Medical Devices and Instrumentation (Wiley, USA, 2006).

2. D. Toomre, J. Pawley, in: J. Pawley (Ed.), Handbook of Biological Confocal Microscopy (Springer, USA 2006) Chapter 10.

3. R. Krishnan, M.J. Heller, J. Biophoton. 2.4, 253–261 (2009)

4. R. Krishnan, D.A. Dehlinger, G.J. Gemmen, R.L. Mifflin, S.C. Esener, M.J. Heller, Electrochem. Comm. 11. 1661-1666. (2009)

5. D. Holmes, H. Morgan, N.G. Green, Biosensors and Bioelectronics. 21. 1621-1630. (2006).

6. T. Jones, Electromechanics of Particles (Cambridge University Press, USA, 1995) Chapters 2,3,5.

7. M.P. Hughes, Nanoelectromechanics in Engineering and Biology (CRC Press, USA, 2003) Chapter 3.

8. P. Ekstrom, in: L.G. Costa, E. Hodgson, D.A. Lawrence, D.J. Reed, Current Protocols in Toxicology (Wiley, USA, 2000) 2.8.1-2.8.21.

9. P. Gascoyne, C. Mahidol, M. Ruchirawat, J. Satayavivad, P. Watcharasit, F.F. Becker, Lab on a Chip. 2. 70-75 (2002).

10. M. Castellarnau, A. Errachid, C. Madrid, A. Juarez, J. Samitier, Biophys. J. 91. 3937-3945. (2006).

11. T. Wu, D. Zhang, J. Chia, K. Tsao, C. Sun, J. Wu, Clinica Chimica Acta. 321. 77-87. (2002)

12. S.N. Mohapatra, K.L. Costeloe, D.W. Hill, Intens. Care. Med. 3. 63-67. (1977).

13. A. Vander, J. Sherman, D. Luciano, Human Physiology: The Mechanisms of Bodily Function. Eighth Edition. (McGraw-Hill, USA, 2001)

14. V. Kumar, H.K. Hagler, Pathologic Basis of Disease. Sixth Edition. (W.B. Saunders Co., USA, 1999)

15. N.C. Seeman, Tibtech. 17. 436-442. (November 1999)

16. J.L. Campos, L. Urpi, T. Sanmartin, C. Gouyette, J.A. Subirana, PNAS. 102.10. 3663-3666. (2005)

17. F.H. Fernandez-Morales, J.E. Duarte, J. Samitier-Marti, Ann. of the Brazilian Acad. Of Sci. 80.4. 627-638. (2008)

18. H.C. Shim, Y.K. Kwak, C. Han, S. Kim, Physica E. 41. 1137-1142. (2009)